ISSN 2744-2640
e-ISSN 2744-2659
JST&M, Vol. 6
www.fipn.unze.ba
10

Journal of **Sustainable Technologies and Materials**

Zenica, June 2026

Journal of Sustainable Technologies and Materials (ISSN 2744-2640)
Vol. 6, No. 10(2026), 1 – 55

Published by
The University of Zenica, Faculty of Engineering and Natural Sciences

Editorial office
Travnička cesta 1,72000 Zenica
Bosnia and Herzegovina
Phone: +387 32 403 468
Email: jstm@unze.ba
Website: https://www.fipn.unze.ba

For submission instructions, manuscript submission, and additional information, please visit https://www.fipn.unze.ba/.

Computer design
Safet Hamedović, University of Zenica, Faculty of Engineering and Natural Sciences

Cover design:
Admir Velić

Printed by „Štamparija Fojnica" D.D.
Fojnica, B&H, in June 2026

Journal of Sustainable Technologies and Materials

JSTM

CONTENTS

JST&M 10(2026), 1– 14
DOI: 10.57131/jstm.2026.10.1

Original scientific paper

ASSESSING ANTIBACTERIAL EFFICACY OF NANOPARTICLES FROM THREE PLANT EXTRACTS AGAINST *E.COLI* AND *STREPTOCOCCI* IN URBAN WASTEWATER

Elton Yerima Ngu[1,2], Julson Ahmed Tchio[3], Kamseu Eli[2], Tsamo Cornelius[1]

[1]Department of Agricultural and Environmental Engineering, College of Technology, University of Bamenda, [2]Laboratory of Materials, Local Materials Promotion Authority, [3]University of Oulu, Fibre and Particle Engineering Research Unit, Finland

ABSTRACT

Silver nanoparticles (Ag-NPs) obtained through green syntheses are gaining remarkable interest in water treatment due to their excellent chemical, physical, and biological properties. Ag-NPs were synthesized using three plant extracts: *Carica papaya*, *Vernonia amygdalina*, and *Perilla frustescens var* as reducing agent, and 6 mM of silver nitrate as precursor. The extracts demonstrated a good potential to reduce Ag(+1) to Ag(0) for Ag-NPs synthesis. Characterization of synthesized Ag-NPs was achieved through UV-Vis spectroscopy, Fourier Transform Infrared analysis, X-ray diffraction, optical microscopy, and zeta potential. The Surface Plasmon Resonance (SPR) was between 410 and 440 nm. The optical microscopy confirmed the presence of nanoparticles (NP) and an aggregate of NP. The synthesized NPs had a crystalline structure, confirmed by the XRD spectra. The average surface charge of NPs was negative (< -10 mV), indicating a potential for aggregation of the three NPs, as confirmed by the particle size distribution. Their antibacterial activities against *E. coli* and *Streptococci* were analyzed in urban wastewater. They exhibited good antibacterial properties, with BNPs being most effective at inhibiting both bacteria, followed by PNP and VNP. This reveals that NPs produced from different plants have different yields, properties, and antibacterial activities, and, most especially, can be used in water and wastewater treatment..

Keywords: *Carica papaya, Vernonia amygdalina*, *Perilla frustescens var*, Ag-NPs, green synthesis, characterization, antibacterial agent

Corresponding Author:
Elton Yerima Ngu,
College of Technology, University of Bamenda
Yaounde - Cameroon
Tel.: 237670803969
E-mail address: nguyerims@gmail.com

1. INTRODUCTION

Nanotechnology has demonstrated diverse applications across a wide range of scientific and technological fields and has emerged as a rapidly growing area of research and innovation. Nanotechnology typically deals with materials possessing at least one dimension below 100 nm [1]. Conventional methods for synthesizing nanoparticles include physical techniques (such as vapor deposition and lithographic processes) and chemical approaches (such as borohydride

and citrate reduction methods). However, these methods often result in relatively large particles with poor monodispersity, and the processes have been reported to pose environmental hazards [2,3]. However, the biological method of synthesis, which is the most recent method, has attracted a lot of attention because it is safe (nontoxic process), cost-effective, and requires less time than other methods [4]. The biological process of synthesizing nanoparticles is mainly through the process of precipitating the nanoparticles of metals like Silver (Ag), Gold (Au), Platinum (Pt), etc., with organic matter like plants, bacteria, and fungi [3, 5].

The area of most interest in the biosynthesis of metal nanoparticles within the last decade is the application of plant extract in the synthesis reaction. Antioxidant biochemicals such as terpenoids, alkaloids, phenolics, aldehydes, proteins, and amino acids are present in plant extracts, which are capable of reducing metal ions to nanoparticles and stabilizing them [6, 7]. Moreover, plants are readily available, hence extracts can be easily obtained, enabling scaling up production. Several documents are available on the development of metal nanoparticles using plant extracts [7, 8-10]. However, silver nanoparticles have emerged to be the most effective because it has a good and broad spectrum of antimicrobial activities against viruses, bacteria, and other microorganisms, and they also have minimal toxicity to human cells [7]. Available reports covering the scope of the modalities to biosynthesize Ag-Nanoparticles of different shapes and characteristics from plant extract have been established [11-14], and their excellent antimicrobial characteristics against: *Staphylococcus aureus, Escherichia coli* [15, 16], *P. aeruginosa*, *K. pneumonia* [16] amongst others, have been observed in cultured mediums. Present interest is in Ag-NP synthesis from three plants, namely: Bitter leaf plant (*Vernonia amygdakina*), Pawpaw plant (*Carica papaya*), and Perilla mint (*Perilla frutescens var*). Extracts from different parts (fruit, leaves, flowers, callus, seed, peel and bark) of these plants have been used for the synthesis of Ag-NP in different studies and they have shown to have incredible antimicrobial and antibacterial properties to bacterial such as: gram-positive and gram-negative bacterial [17-19], *E-coli* and *Staphyloccocus* [20-22]; coliform [23], oral bacterial [24], anticancer [22, 25] and also in colorimetric experiments to determine heavy metals in solution [26]. Even though there is some study on the application of Ag-NP produced from these three plants in inhibiting microbial or bacterial action or eliminating them, it has mostly been applied in the medical domain and in controlled environments, such as diffusion methods. Also, there are few or no studies available on the application of Ag-NP produced from these plants in industrial, urban, or domestic wastewater treatment.

The present study aims to achieve the following objectives:

1. Synthesize silver nanoparticles from three different plants: *Carica papaya* (Paw-paw plant), *Vernonia amygdalina* (Bitter leaf plant), and *Perilla frustescens var* (Perilla mint plant).
2. Characterize the silver nanoparticles by UV-VIS spectroscopy, Fourier-transformed infrared spectroscopy (FTIR), X-ray diffraction, and zeta potential.
3. To compare the antibacterial properties of the silver nanoparticles against *E.coli* and *Streptococcus* in domestic wastewater.

The key findings of this work are related to the comparative study of the antibacterial activities of Ag-reduced nanoparticles using three plant extracts.

2. MATERIALS AND METHODS

2.1. Collection of plant materials

The samples of interest for synthesizing silver nanoparticles were from three different plant types. The paw-paw plant (*Carica papaya*), bitter leaf plant (*Vernonia amygdalina*), and Perilla mint plant (*Perilla frutescens var*). These plants were selected

because they are traditionally regarded as medicinal plants in rural Cameroon and are used in the treatment of diseases such as typhoid fever, hemorrhoids, ringworm, and various other ailments. Plant samples were obtained from a farmland around the military base in Yaounde, commonly known as "Quartier Gènèral". To ensure consistency of content and reproducibility of results, a one-time sampling was done around the sample area, where for each plant, several samples were jointly collected. The plants were washed with deionized water 3-4 times and exposed to sunlight for about 14 days to lose humidity and dry up. Samples were rewashed to remove dust particles that may have accumulated during drying. The samples were then placed in an oven at 50 °C to dry slowly. After drying, samples were crushed and preserved in labeled plastic bags.

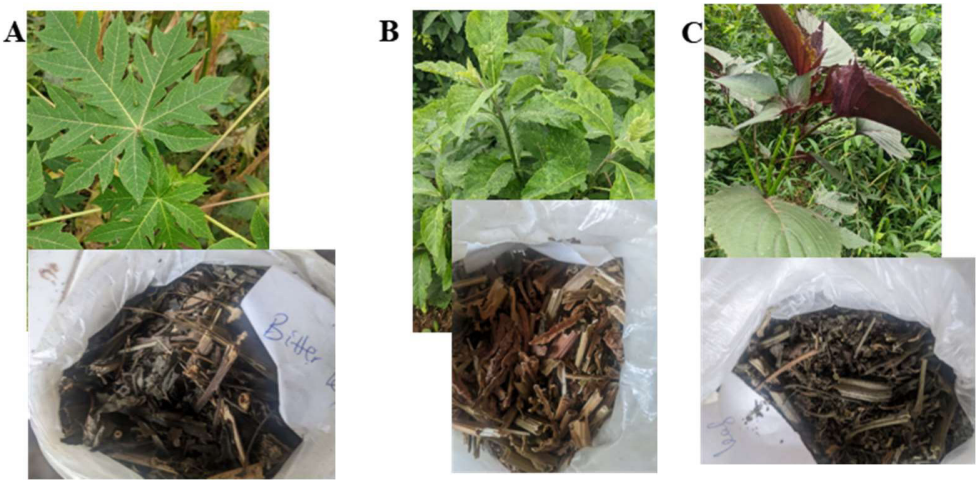

Figure 1. Plant Samples used in the synthesis of Ag-NPs: (A) *Carica papaya*: (Pawpaw plant); (B) *Vernonia amygdalina*: (Bitter leaf plant); (C) *Perilla frutescens var*: (Perilla mint plant)

2.2. Collection of extracts from plants and preparation of a solution

Plant extracts were obtained using an adopted and modified procedure from Maged et al. [15]. 20 g of each crushed plant sample was placed in a 1000 ml Erlenmeyer flask, and 400 mL of deionized water was added to it. The flask and its content were then placed on a heater at 60 °C and stirred at 500 rmp for 60 minutes (1 hour). When the color of the solution turned brown, it was allowed to cool at room temperature, then filtered with a Whatman filter paper to remove all plant particles. The extracts were then preserved at 4 °C to be used later for bio-nanoparticle synthesis.

According to Maged et al. [15], the concentration of silver nitrate with optimal reduction characteristics and the best antibacterial properties is 6 mM. Analytical grade Silver Nitrate reagent (99.5% purity level), was commercially purchased. The silver salt used did not need any further purification. Distilled water was used to make the solution. A solution of silver nitrate with the prescribed concentration was prepared by dissolving the appropriate amount of the silver salt into distilled water, stirring until the solution was homogeneous, and sealing the solution to prevent any contamination.

2.3. Biosynthesis and characterization of Silver nanoparticle (Ag-NP)

The Ag NP were synthesized by putting 2 mL of leaf extract in their respective labeled sample container. 50 mL of 6 mM silver nitrate solution was added to the leaf extract and allowed to sit at room temperature. The

reaction was followed up for over a period of 4 hours.

The composition, size, and morphology of the synthesized Ag-NPs were determined through various characterization methods. To determine the formation of Ag-NPs, UV-VIS spectrometry was done on each sample after 24 hours. A quartz cuvette with a 1 cm optical path was used with a wavelength range of 300 – 600 nm. The morphology and size of the Ag-NPs were observed by means of optical microscopy. For evidence of Ag in the nanoparticles, X-ray diffraction analysis was done on the Ag-NPs.

2.4. Characterization of antibacterial properties of nanoparticles

For characterization of the nanoparticle's antibacterial properties, the nanoparticles were used to treat domestic wastewater. Wastewater was sampled from a municipal waste stream in Bonamoussadi, Yaounde, Cameroon. Six plastic bottles were cleaned with distilled water, and into each container, 1 L of the wastewater sample was introduced. 30 mL of nanoparticle solution from the three plant extracts was poured into three containers, each in its own container, and labeled: VL1 (wastewater + Perilla mint NP), PP1 (Wastewater + Pawpaw plant NP), and BL1 (wastewater + Bitter leaf NP). An equivalent amount (30 mL) of silver nitrate in one container (Ag(1+): Wastewater + AgNO3) and finally plant extract in another (EXT: wastewater + Plant extract). A container of wastewater (WW) was used as a reference. Each container and its contents were allowed to stand for 24 hours at room temperature. The cup-plate agar diffusion method was used to E-coli and Streptococci load in water samples [15].

3. RESULTS AND DISCUSSION

The study on the green synthesis of Ag nanoparticles using bitter leaf plant, pawpaw plant, and Perilla plant extracts was done and systematically reported in this report. The aqueous Ag+ was reduced to silver nanoparticles upon the addition of natural plant extracts. The colors observed during the transition of the reaction were from pale yellow to a brown solution with precipitate settling at the bottom of the solution within 5 hours of reaction. No further changes were detected for another 12 h; however, the majority of the precipitates had settled, and the solution became clearer.

3.1. UV-VIS characterization

The confirmation of the formation of silver nanoparticles was monitored using UV-VIS spectrometric analysis (UV752(D) PEC Medical USA UV/VIS photospectrometer). The UV-VIS spectra (Figure 2) of silver nanoparticles from the three plant extracts showed an increase in absorbance with an increase in wavelength from 300-600 nm, with an intense Surface Plasmon Resonance (SPR) observed at 410 and 440 nm, and are in the range for the stipulated absorption wavelength of Silver. This conforms to the findings of Logeswari et al [16], who indicated that the maximum absorption of silver nanoparticles within this wavelength range confirms their formation. Furthermore, the band of the silver nanoparticles spectra was similar, which would indicate a similarity in average particle size and shape as stipulated by Bamsaoud et al. [27] and Mage et al. [15]. However, the absorption peak of Pawpaw extract Ag-nanoparticles (PNP) was identified to have a red shift and decrease in intensity, which could be attributed to the increase in particle size of this nanoparticle, compared to the other two. Furthermore, the alignment of the peaks of BNP and VNP would indicate their particle size falls within the same range; however, given that the absorption peak of BNP is more intense, this might insinuate the high concentration of BNPs, which are more stable with the smallest size compared to the other two [28]. Hence, the UV-VIS absorption peak reveals that nanoparticles produced from bitter leaf plant extract (BNP) are more stable, with a quick formation of nanoparticles, a higher concentration of nanoparticles, and the

smallest size. This is closely followed by nanoparticles produced from Perilla extract (VNP), and finally, those from pawpaw plant extract (PNP). This would indicate that different plants subjected to the same conditions for the green synthesis of nanoparticles have different formation kinetics, size, and shape. This difference in formation kinetics might be attributed to the unique phytochemicals of each plant based on the concentration of reducing agents (polyphenol, flavonoids, and tannins) in each plant [29].

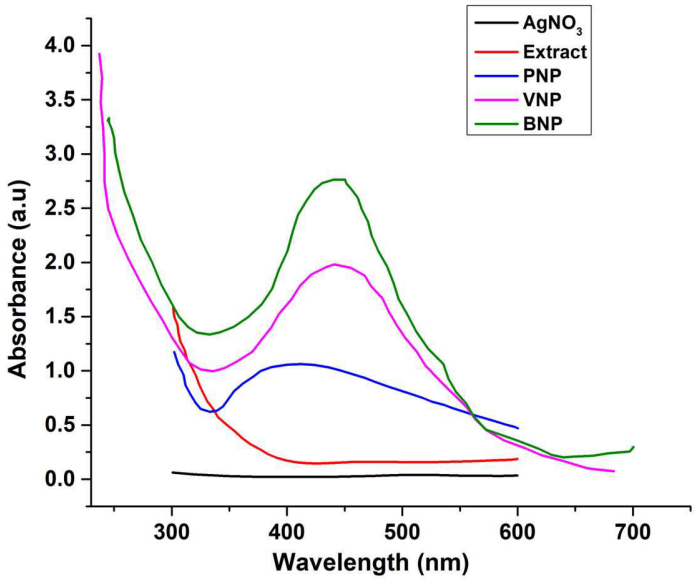

Figure 2. UV-VIS Spectra of Silver nitrate ($AgNO_3$), Plant extract (Extract), and Ag-NPs (PNP, VNP, BNP), *PNP: Pawpaw plant Ag-nanoparticles; VNP: Perilla plant Ag-NP; BNP: Bitter leaf plant Ag-NP*

The UV-VIS spectroscopic analysis also has the possibility of determining the size and shape of nanoparticles. The absorption spectra of the synthesized nanoparticles revealed peaks in the range of 410 – 440 nm. According to Martínez-Castañón et al. [30], nanoparticles with absorptions within this range are mostly characterized by a spherical shape and a size range between 7 and 30 nm. Which fall within the size range of nanoparticle materials.

3.2. Fourier Transform Infrared (FTIR) Spectroscopy analysis

The FTIR analysis investigates and identifies the functional groups present in both plant extract and Ag-NPs, as well as reveals factors responsible for capping and possible interactions between silver and bioactive molecules. The FTIR spectrometry data were obtained at the inorganic laboratory of the University of Yaounde 1 (Cameroon) using the BURKER OPTIK ALPHA Spectrometer (standard glass cells and Borosilicate glass windows). This analysis depends on the principle that electromagnetic energy in the infrared region, ranging from 4000 – 400 cm^{-1}, is absorbed by particles, causing the subatomic particles to vibrate. Figure 5 presents the FTIR spectrograph of the synthesized Ag-NPs from all three plants. Based on the FTIR peaks characterization, the peak position reveals the form of nanoparticles, while the intensity of the peak determines the size of the nanoparticles [31, 32]. The FTIR spectrum reveals a broad and intense band from 3800-3000 cm^{-1} with a peak at around 3302 cm^{-1}, which may probably be due to the stretching or bending vibration of the hydroxyl groups (O-H) of polyols such as Glycerol, Mannitol, hydroxyflavones, and catechins, or the vibration of O-H of water

molecules on the surface of the Ag-NPs [33]. Absorption band at 1636 cm^{-1} may correspond to the C=O stretching vibration of the carbonyl group (-C=O), which may indicate either the presence of carboxylic acids or amides [34, 35]. These phytochemicals have been reported to be present in plant extracts and are primarily responsible for the bioreduction of Ag ions to Ag-NPs, contributing to their stabilization and the provision of a capping agent that prevents agglomeration of Ag-NPs [36, 37]. Finally, the peak at 415 cm^{-1} could be attributed to the stretching vibration of Ag-O of silver oxide or might suggest interactions between silver nanoparticles (Ag-NPs) and oxygen-containing functional groups in accordance with the findings of Kayed et al. [38]. This might also imply the stabilization of Ag-NPs by organic compounds containing oxygen.

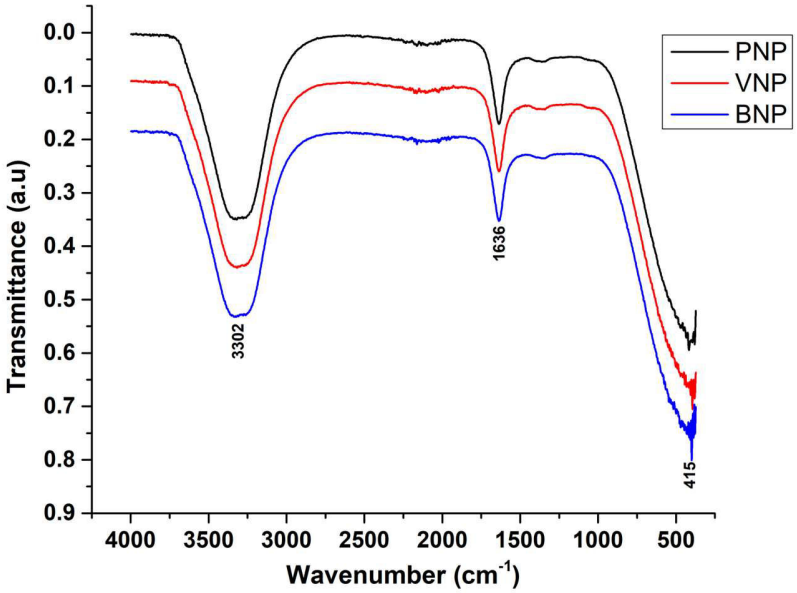

Figure 3: FTIR analysis of synthesized Ag-NPs

3.3. X-ray Diffraction analysis

This analysis is an essential technique to determine the crystalline nature of the nanoparticles. X-ray analysis was done in the Department of Engineering Enzo Ferrari University of Modena. It was performed using a Bruker D8 Discover, Japan, Cu-Kα radiation at 40 kV and 30 mA, θ to 2θ configuration. Spectral measurements were performed in the angular range of 5°–80° (2θ/min). Figure 4 shows the X-ray diffractogram of the Ag-NP produced from the three plant extracts, to confirm their crystal characteristics. The diffractogram of the Ag-NPs confirmed its crystalline characteristics. Major peaks were observed around the following angles; 23.02°, 26.4°, 34.4°, 37.86°, 40.68°, 49.12°, 54.2°, 56.56°, and 76.06°. Referencing from the International Center for Diffraction Data (ICDD), these peaks corresponds to the silver crystalline phases in the plane (111), (220), (200), (220), (311), (222), (440) respectively, and are attributed to the face-centered cubic (FCC) crystal structure. These results corroborated the data obtained from the standard ICDD database having card no: #00-004-0783. Of all the phases, the most important is the (111) plane configuration, which indicates the Ag-NPs are well crystalline and stable. The unassigned peaks phases marked "X" and others in the figure may be due to the crystallization of bioorganic phases present in these plants, according to Asif et al. [39].

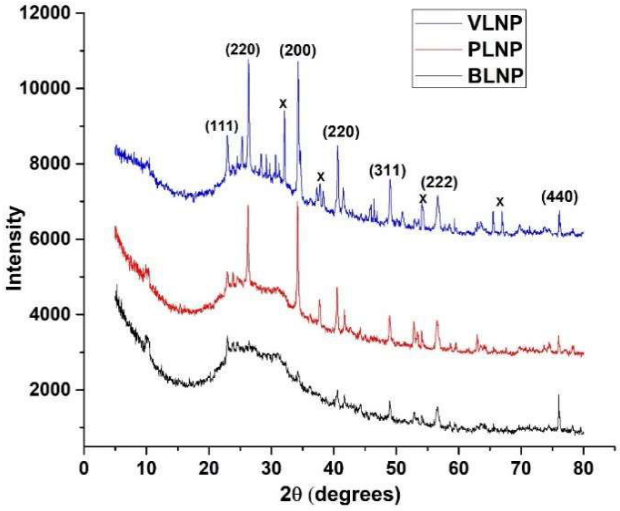

Figure 4. X-ray diffractogram of synthesized Ag-NPs

3.4. Microscopy of Silver nanoparticles

Microscopy is a surface imaging method that is essential in determining the particle size distribution, particle structure, and surface morphology of the synthesized nanoparticle. In this study, optical microscopy was used to determine the morphology of the Ag-NP from the three plant extracts (Figure 5). The optical microscopy was done in Oulu University, Finland, using Dark-field microscopy (DFM). It operates through selectively capturing light scattered from the sample while excluding the incident light. As a result, the field around the sample produces a dark background while the sample is visualized as a bright object [40, 41]. Observations were done at 250 µm, 100 µm, and 50 µm. It could be observed that the Ag-NPs from the 3 plant extracts were formed, which are dense, not too dispersed, and agglomerated in certain regions, with different sizes of nanoparticles. Agglomerations could be a result of the solvent effect of Van der Waals attraction between particles in solution, causing them to form little clusters. Optimal microscopic analysis was only able to observe the presence of nanoparticles in solution. However, scanning electron microscopy (SEM) and transmission electron microscopy (TEM) are required to observe a more detailed surface morphology of the nanoparticles for their shape and size.

3.5. Particle size distribution and Zeta potential analysis

This is an essential analysis that determines the electrical potential of nanoparticles in colloidal dispersions to define their charge in suspension. Zeta potential was measured by adding Ag-NP solution to a cell that contains two gold electrodes. When a voltage was applied to the electrode, the particles moved towards the electrode with the opposite charge. A Doppler technique was used to measure the particle velocity as a function of voltage. A laser passes through the cell, and as particles move through the laser beam, the intensity of scattered light fluctuates at a frequency proportional to the particle speed. Particle speed at multiple voltages was measured, and the data were used to calculate the zeta potential. This reveals the surface charge, stability, and aggregation of nanoparticles. The average zeta potential of the synthesized nanoparticles was -7.142 mV, -6.082 mV, and -1.424 mV for BLNP, PLNP, and VLNP, respectively (Figure 6).

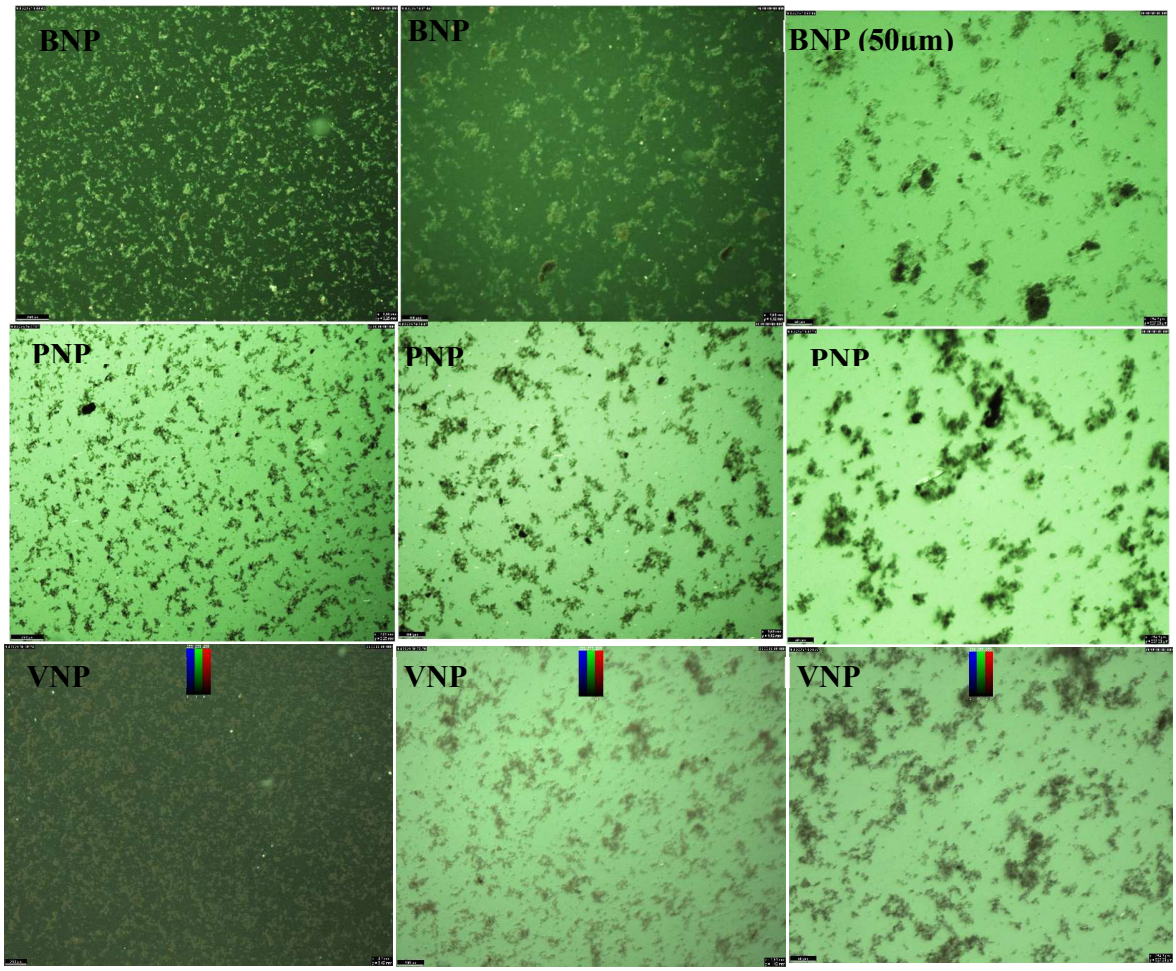

Figure 5. Optical microscopic imaging of synthesized nanoparticles: *BNP (Bitter leaf plant extract NP), PNP (Pawpaw plant extract NP),* and *VNP (Perilla mint extract NP)*

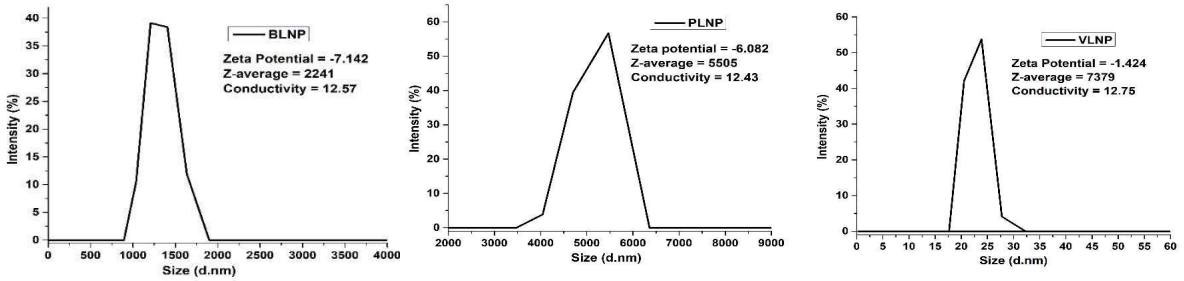

Figure 6. Particle size distribution – Zeta potential of synthesized nanoparticles

The negative zeta potential of the Ag-NPs would indicate that the net charge on the surface of the nanoparticles is negative. Furthermore, the values were observed to be less than 10 mV, indicating the nanoparticles are unstable with weak repulsion forces between suspended particles, limiting dispersion [42]. This may be an indication of the high particle size values of the synthesized particles, given that there was an

aggregation of particles, which confirms the microscopy observations. However, Ag-NP produced from bitter leaf (BLNP) had the highest potential, indicating it has the most stability, while VLNP had the least potential, indicating the least stability of the three synthesized Ag-NPs.

3.6. Evaluation of antibacterial properties of nanoparticles

The antibacterial efficiency of silver nanoparticles has been mostly observed either in medical applications, microbial incubated treatment [15, 27], or cultured bacterial treatment [3], where nanoparticles are being used to treat one, at most three microbes at a time. However, there is very limited literature or works on the determination of antibacterial properties of silver nanoparticles in standard wastewater. The silver nanoparticles (Ag-NP) synthesized in this study were tested for their efficiency to eliminate *E. coli* and *Fecal Streptococci* from domestic wastewater. Figure 7 presents the effect of synthesized silver nanoparticles, plant extract used for nanoparticles synthesis, and silver nitrate in wastewater on bacteria in domestic wastewater. Three groups of tests were carried out: nanoparticles in wastewater (VL1, PP1, and BL1), plant extract in wastewater (EXT), and silver nitrate in wastewater (Ag(+1)). The antibacterial properties were evaluated for two bacteria, *E. coli* and *Fecal Streptococci*. When the silver nanoparticles and silver nitrate were introduced into wastewater, the color of the mixture changed from grey to a deep red solution (VL1, PP1, and BL1), but brown for the wastewater in which silver nitrate was added (Ag(1+)) (Figure 7). The change in this color might be due to the influence of their optical properties, due to interactions of the organic and inorganic composition in wastewater, and the Ag (0) and Ag (+), affecting the aggregation and dissolution of NPs, which is in accordance with the findings of Gibson (2018). Alternatively, this might be due to the formation of larger nanoparticles as a result of the reduction of the remaining Ag (+) in solution to Ag (0) by organic contents in water, resulting in a darker solution [43, 44].

Figure 7. Appearance of wastewater upon addition of green-synthesized nanoparticles; *WW: Raw wastewater, EXT: Wastewater + Extract, AG(1+): Wastewater + $AgNO_3$, VL1, PP1, BL1: Wastewater + Silver nanoparticles*

Figure 8 presents the antibacterial analysis of the treated wastewater samples and the wastewater. Figure 8A presents the inhibition zones of Ag-NP on E. coli. It could be observed that the highest inhibition was found in BL1 (BL1 (*E-coli*)), followed by PP1 (PP1 (*E-coli*) and VL1. WW and EXT had high concentrations of *E. coli* (little or no inhibition). Figure 8B presents the inhibition zones of Streptococci in the samples. It could be observed that the highest inhibition of Streptococci was in BL1, followed by VL1, PP1, and Ag (1+). The highest concentrations of *Streptococci* were found in WW.

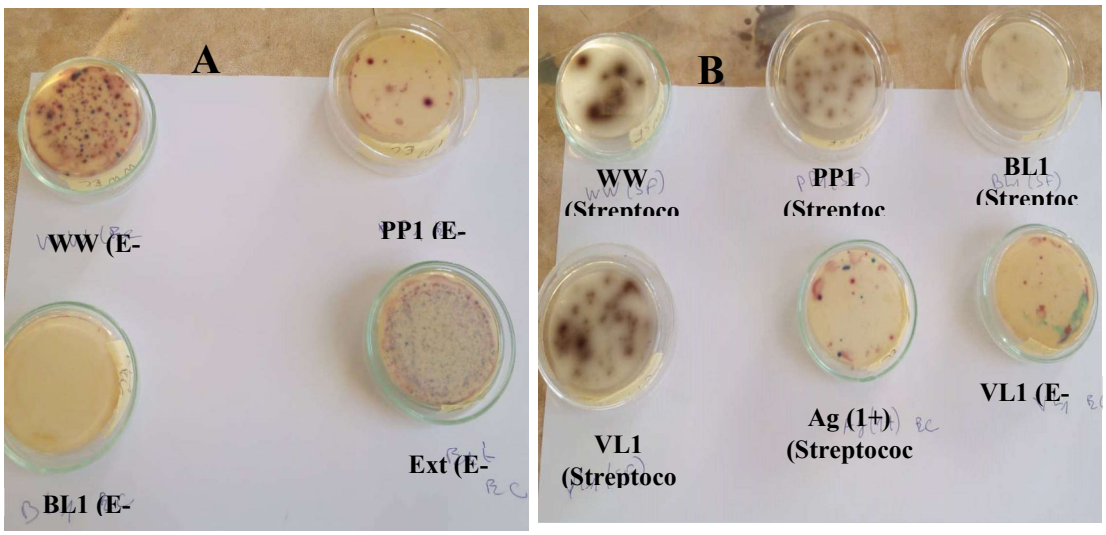

Figure 8. Diffusion analysis of the wastewater and treated water samples against (A) *E. coli*, (B) *Streptococci*

From raw wastewater analysis, it was observed that the mean count for *Fecal Streptococci* (FS) was 12 x 103 CFU/100 ml and *Escherichia coli* (EC) was 47 x 103 CFU/100 ml. These counts decreased with the addition of nanoparticles produced from the three plant extracts and silver nitrate, but remained unchanged with the addition of the plant extracts.

Figure 9 presents the *E. coli and Streptococcus bacterial counts in all water samples, corresponding to the nanoparticles' ability* to eliminate each bacterium. It can be observed from the analysis that the mean value of the *E. coli* was relatively high in the raw wastewater, and was reduced upon addition of the different nanoparticles and AgNO3 solution. The *E. coli* elimination efficiency for the various nanoparticles were 99.6% for the nanoparticles produced with paw-paw plant (PNP), 98.1% with Perilla mint nanoparticles (VNP), and 100% removal efficiency with the bitter leaf nanoparticles (BNP). The AgNO3 solution was observed to have an E. coli elimination efficiency of 89.8%. The highest elimination efficiency of *E. coli* was

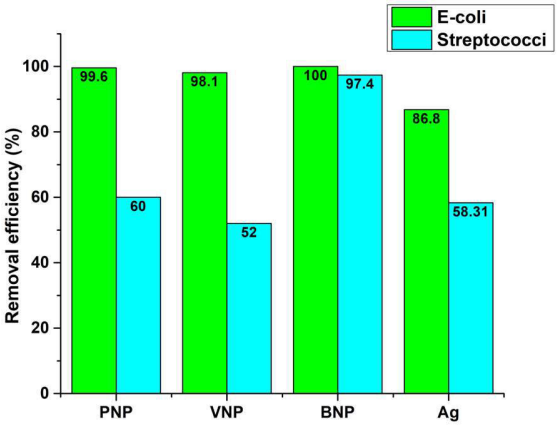

Figure 9. Antibacterial activities of Ag-NP against *E. coli* and *Streptococci*

obtained from the silver nanoparticles produced with bitter leaf (BNP).

Similarly, with the addition of Silver nanoparticles produced from various plant extracts, the counts of Streptococci reduced with an elimination efficiency of 60% in PNP, 52.5% in VNP, and 97.42% in BNP. Furthermore, the *Streptococci* elimination efficiency for $AgNO_3$ solution was found to be 58.31%. The addition of each plant extract had no notable effect on the microbes in wastewater.

The observed results indicate that the synthesized Ag-NPs are suitable for inhibiting the activities of microorganisms like *E. coli*, *Streptococci,* and possibly other microbes in wastewater. The aforementioned results also reveal that Ag-NPs synthesized from the different plants had different degrees of antibacterial activities on different microbes, and the Ag-NPs produced from bitter leaf (BNP) had the highest antibacterial activity of the three. This confirms that, as the phytochemistry of the plant affects its kinetics of production, so does it affect its antibacterial properties. The use of Ag-NP will therefore find extensive use in water and wastewater treatment.

4. CONCLUSION

In the synthesis of metal nanoparticles through bio-reduction, silver nanoparticles (Ag-NPs) have gained a lot of interest due to their formidable properties and good antimicrobial characteristics. This study seeks to determine the characteristics and antibacterial properties of Ag-NPs produced from different plants. Three plants were selected, ie, *Carica papaya* (Paw-paw plant), *Vernonia* amygdalina (Bitter leaf plant), and *Perilla frustescens var* (Perilla mint plant) as reducing and capping agent, and 6 mM silver nitrate as precursor. The synthesized NPs were characterized through optical microscopy, UV-Vis spectroscopy, FTIR, XRD, particle size distribution, and zeta potential. The confirmation of the formation of Ag-NPs was revealed by the UV-Vis spectroscopy, with the Surface Plasmon Resonance between 410 and 440 nm, and the most intense being VNP and BNP. XRD revealed the strong crystalline nature of the Ag-NPs synthesized from all three plant extracts. The optical microscopy observation of Ag-NPs showed the presence of NPs formed, slightly dispersed with zone aggregation. By means of zeta potential, it was seen that the average surface charge of all the nanoparticles was negative, and less than -10 mV, indicating weak inter-repulsion between nanoparticles, hence strong affinity for aggregation. This was confirmed through their particle size distribution. In the treatment of urban wastewater, all three Ag-NPs had the affinity to eliminate *E. coli* and *Streptococci* in wastewater. BNP had the best inhibiting capacity, followed by PNP and finally VNP. Hence, NP produced in the same conditions from different plant extracts exhibit different degrees of antibacterial properties. In summary, the application of biosynthesized nanoparticles can pass its laboratory phase into a standard water and wastewater treatment system.

Acknowledgement

The authors thank the Local Materials Promotion Authority (MIPROMALO) for providing laboratory facilities to carry out this research.

Funding

The authors of the manuscript did not receive any funding or grants for this work.

Credit authorship contribution statement

Elton Yerima: Investigator, Writing-Original draft. **Julson Ahmed Tchio**: Analysis. **Tsamo Cornelius**: Supervisor and conceptualization. **Elie Kamseu**: Supervisor.

Conflict of Interest

The authors declare that they have no known competing financial interests or personal relationships that could have appeared to influence the work reported in this paper.

5. REFERENCES

[1] B. K. Narayanan, S. Natarajan, Biological synthesis of metal nanoparticles by microbes, *Adv. Colloid Interface Sci.*, 156 (2010), pp. 1–13

[2] P. Mukherjee, M. Roy, B. P. Mandal, G. K. Dey, P. K. Mukherjee, J. Ghatak, A. K. Tyagi, S. P. Kale, Green synthesis of highly stabilized nanocrystalline silver particles by a non-pathogenic and agriculturally important fungus *T. Asperellum*, *Nanotechnol.*, 19 (2008) 7, doi 10.1088/0957-4484/19/7/075103p 7.

[3] T. M. Mohammed, Removal of pathogenic bacteria from wastewater using silver nanoparticles synthesized by two fungal

species, *Water Science*, 31 (2017) 2, https://doi.org/10.1016/j.wsj.2017.11.001

[4] V. Arya, Living systems eco-friendly nanofactories, *Dig. J. Nanomater. Biostruct.*, 5 (2010) 1. pp 9–21

[5] D. M. Ali, M. Sasikala, M. Gunasekaran, N. Thajuddin, Biosynthesis and characterization of silver nanoparticles using marine Cyanobacterium oscillatoria, *Dig. Journal of Nanomater. Biostruct*, 6 (2011) 2, pp 385–390

[6] R. E. Sardjono, R. Gunawan, B. Anwar, Erdiwansyah, R. Mamat, A Mini Review: Biosynthesis of Silver Nanoparticles and Its Activity as Antioxidant, *Moroccan Journal of Chemistry,* 10 (2022) 4. pp 808–821. https://doi.org/10.48317/IMIST.PRSM/morjchem-v10i3.30801

[7] S. Anjum, J. Gideon, G. Bhuvanesh, Investigation of the herbal synthesis of silver nanoparticles using Cinnamon zeylanicum extract, *Emergent Materials*, 2 (2019), pp 113–122, https://doi.org/10.1007/s42247-019-00023-x

[8] J. Bhaumik, N. S. Thakur, P. K. Aili, A. Ghanghoriya, A. K. Mittal, U. C. Banerjee, *ACS Biomater. Sci. Eng.*, 1 (2015) 6, p. 382

[9] N. S. Thakur, J. Bhaumik, S. Kirar, U. C. Banerjee, *ACS Sustain. Chem. Eng.*, 5 (2017) 9, p. 7950

[10] S. Y. Lee, S. Krishnamurthy, C. W. Cho, Y. S. Yun, Biosynthesis of gold nanoparticles using *Ocimum sanctum* extracts by solvents with different polarity, *ACS Sustain. Chem. Eng.*, 4 (2016) 5, pp. 2651–2659, https://doi.org/10.1021/acssuschemeng.6b00161

[11] M. Bahwirth, S. Bamsaoud, The effect of silver nanoparticles on the germination and growth of two cultivars of wheat, *Triticum aestivum* L. Alandalus, *Journal of Applied Science*, 7 (2020) 11, pp. 7–25

[12] S. F. Bamsaoud, M. A. Bahwirth, The effect of biologically synthesized silver nanoparticles on the germination and growth of *Cucurbita pepo* seedlings, *Journal of the Arab American University*, 3 (2017) 2, pp. 34– 47

[13] T. Tenzin, A. Kaur, Recent Advances in the Green Synthesis of Gold and Silver Nanostructures for Augmented Anti-Microbial Activity, *Iranian Journal of Materials Science and Engineering*, 19 (2022) 2, pp. 1- 28 https://doi.org/10.22068/ijmse.2252

[14] S. Dimitrieska, A. Stankovska, T. Efremova, The Fourth Industrial Revolution Advantages and Disadvantages, *Economics and Management*, 14 (2018) 2, pp. 182–187

[15] M. M. Basuliman, A. S. Bamahel, D. G. Al-Kathiri, A. M. Al-Suhily, The Effect of Various Concentrations of $AgNO_3$ Aqueous Solutions on Silver Nanoparticles Biosynthesis Using *Tarchonanthus Camphoratus* Leaf Extract and Their Antibacterial Activity, *Mor. Journal of. Chememistry*, 14 (2023) 2, pp. 361-370. Doi: https://doi.org/10.48317/IMIST.PRSM/morjchem-v11i1.33269

[16] P. Logeswari, S. Silambarasan, J. Abraham, Synthesis of silver nanoparticles using plant extract and analysis of their antimicrobial property, *Journal of Saudi Chemical Society,* 19(2012) 3, pp. 311-317 http://dx.doi.org/10.1016/j.jscs.2012.04.007

[17] E. S. H. Haridas, M. K. R. Varma, G. K. Chandra, Bioactive silver nanoparticles derived from *Carica papaya* floral extract and its dual-functioning biomedical application, *Science Report,* (2025) 15, p. 9001 https://doi.org/10.1038/s41598-025-93864-y

[18] G. Z. Jahangir, T. Anjum, N. Rashid, M. Sadiq, R. Farooq, M. Akhtar, S. Hussain, A. Iftikhar, M. Z. Saleem, R. S. Shaikh, *Carica papaya* Crude Extracts are an Efficient Source of Environmentally Friendly Biogenic Synthesizers of Silver Nanoparticles, *Sustainability,* 15(2023) 24, p. 16633, https://doi.org/10.3390/su152416633.

[19] R. C. Omeh, I. J. Ali, C. C. Adonu, *Venonia amygdalina* leaf extract - mediated redox synthesis of silver nanoparticles: Characterization and antimicrobial activity, *German Journal of Pharmaceuticals and Biomaterials*, 2 (2023) 4, pp. 19-30

[20] J. Balavijayalakshmi, V. Ramalakshmi, *Carica papaya* peel mediated synthesis of silver nanoparticles and its antibacterial activity against human pathogens, *Journal of Applied Research and Technology,* 15 (2017) 5, pp. 413-422 https://doi.org/10.1016/j.jart.2017.03.010.

[21] A. C. Ovenseri, O. A. Johnbull, Formulation of silver nanoparticles from the leaves extract of *Vernonia amygdalina*, *The Nigerian Journal of Pharmacy*, 57 (2023) 1, pp. 459 – 466, https://doi.org/10.51 412/psnnjp.2023.7

[22] M. Tavan, P. Hanachi, M. H. Mirjalili et al., Comparative assessment of the biological activity of the green synthesized silver nanoparticles and aqueous leaf extract of *Perilla frutescens* (L.), *Science Report,* 13 (2023), 6391 https://doi.org/10.1038/s41598-023-33625-x

[23] S. O. Aisida, K. Ugwu, P. A. Akpa, A. C. Nwanya, U. Nwankwo, S. S. Botha, P. M. Ejikeme, I. Ahmad, M. Maaza, F. I. Ezema, Biosynthesis of silver

nanoparticles using bitter leaf (*Veronica amygdalina*) for antibacterial activities, *Surfaces and Interfaces*, 17 (2019), 100359– https://doi.org/10.1016/j.surfin.2019.100359.

[24] A. A. O. Sirajudeen, J. F. Sanusi, O. A. Akintola, A. O. Sakariyau, O. F. Adesina, S. Bankole, Eco-Friendly Production of Silver Nanoparticles from *Vernonia amygdalina* and *Citropsis articulata*: An Assessment of Antibacterial Properties against Oral Bacteria, *Journal of Medical Microbiology and Infectious Diseases*, 12 (2024) 1, pp. 22 -34 https://doi.org/10.61186/JoMMID.12.1.22. ,

[25] T. Hou, Y. Guo, W. Han, Y. Zhou, V. R. Netala, H. Li, H. Li, Z. Zhang, Exploring the Biomedical Applications of Biosynthesized Silver Nanoparticles Using *Perilla frutescens* Flavonoid Extract: Antibacterial, Antioxidant, and Cell Toxicity Properties against Colon Cancer Cells, *Molecules, 28* (2023), 17, pp. 6431 https://doi.org/10.3390/molecules28176431

[26] M. Firdaus, S. Andriana, Elvinawati, W. Alwi, E. Swistoro, A. Ruyani, A. Sundaryono, Green synthesis of silver nanoparticles using *Carica Papaya* fruit extract under sunlight irradiation and their colorimetric detection of mercury ions. *Journal of Physics: Conference Series*, 817 (2017) 1, 012029 https://doi.org/10.1088/1742-6596/817/1/012029

[27] S. F. Bamsaoud, M. M. Basuliman, E. A. Bin-Hameed, S. M. Balakhm, A. S. Alkalali, The effect of volume and concentration of $AgNO_3$ aqueous solutions on silver nanoparticles synthesized using *Ziziphus Spina* – Christi leaf extract and their antibacterial activity, *Journal of Physics: Conference Series*, Volume 1900, The 1st International Conference on Fundamental, Applied Sciences and Technology (ICoFAST 2021), 15-16 March 2021, (Perlis, Malaysia), (Hadhramout, Yemen) https://doi.org/10.1088/1742-6596/1900/1/012005.

[28] R. Sarkar, P. Kumbhakar, A. K. Mitra, Green Synthesis of Silver Nanoparticles and Its Optical Properties, *Digest Journal of Nanomaterials and Biostructures*, 5 (2010) 2, pp. 491 – 496

[29] M. Ansari, S. Ahmed, A. Abbasi, M. T. Khan, M. Subhan, N. A. Bukhari, A. A. Hatamleh, N. R. Abdelsalam, Plant-mediated fabrication of silver nanoparticles, process optimization, and impact on tomato plant, Scientific Reports, 13(2023):18048 https://doi.org/10.1038/s41598-023-45038-x.

[30] G. A. Martínez-Castañón, N. Niño-Martínez, F. Martínez-Gutiérrez, J. R. Martínez-Mendoza, F. Ruiz, *Journal of Nanoparticle Resources*, 10 (2008), 1343

[31] S. Pugazhendhi, P. Sathya, P. K. Palanisamy, R. Gopalakrishnan, Synthesis of silver nanoparticles through green approach using *Dioscorea alata* and their characterization on antibacterial activities and optical limiting behavior, *Journal of Photochemistry and Photobiology B: Biology*, 159 (2016), pp. 155-160

[32] E. A. A. Kareem, H. M. Oraibi, A. E. Sultan, Synthesis and Characterization of Silver Nanoparticles: A Review. *Ibn Al-Haitham Journal for Pure and Applied Sciences*, IHJPAS.. 36 (2023) 3, https://doi.org/10.30526/36.3.3050.

[33] N. Jain, A. Bhargava, S. Majumdar, J. C. Tarafdarb, J. Panwar, *Nanoscale*, 3 (2011), 635

[34] D. T. Stalin, In vitro antibacterial activity of biosynthesized silver nanoparticles against Gram-negative bacteria, *Inorganic and Nano-Metal Chemistry*, 2022, pp. 1-10.

[35] Z. Hashemi, Z. M. Mizwari, S. Mohammadi-Aghdam, S. Mortazavi-Derazkola, M. A. Ebrahimzadeh, Sustainable green synthesis of silver nanoparticles using *Sambucus ebulus phenolic* extract (AgNPs@ SEE): Optimization and assessment of photocatalytic degradation of methyl orange and their in vitro antibacterial and anticancer activity, *Arabian Journal of Chemistry,* 15 (2022) 1, 103525

[36] S. Palithya et al., Green synthesis of silver nanoparticles using flower extracts of *Aerva lanata* and their biomedical applications, *Particle Science and Technol.,* 40 (2022) 1, pp. 84–96

[37] A. Dhaka, S. C. Mali, S. Sharma, R. A.Trivedi, Review on biological synthesis of silver nanoparticles and their potential applications, *Results in Chemistry,* 6 (2023) 101108 https://doi.org/10.1016/j.rechem.2023.101108

[38] K. Kayed, M. Issa, H. Al-ourabi, The FTIR spectra of Ag/Ag_2O Composites Doped with Silver Nanoparticles, *Journal of Experimental Nanoscience,* 19 (2024) 1, 2336227 https://doi.org/10.1080/17458080.2024.2336337

[39] M. Asif, R. Yasmin, R. Asif, A. Ambreen, M. Mustafa, S. Umbreen, Green Synthesis of Silver Nanoparticles (AgNPs), Structural Characterization, and their Antibacterial Potential, *Dose-Response: An International Journal*, 20 (2022) 2 https://doi.org/10.1177/15593258221088709

[40] L. W. Zhang, N. A. Monteiro-Riviere, Use of confocal microscopy for nanoparticle drug

delivery through skin, *Journal of Biomedical Optics,* 18(2013) 6:061214. https://doi.org/10.1117/1.JBO.18.6.061214

[41] A. Al-Zubeidi, L. A. McCarthy, A. Rafiei-Miandashti, T. S. Heiderscheit, S. Link, Single-particle scattering spectroscopy: fundamentals and applications, *Nanophotonics*, 10 (2021) 6, pp. 1621–1655 https://doi.org/10.1515/nanoph-2020-0639

[42] Malvern. Technical notes: Zeta potential – Introduction in 30 minutes. Malvern Instrument Limited. 2015, https://www.research.colostate.edu/wp-content/uploads/2018/11/zetapotential-introduction-in-30min-Malvern.pdf. (Accessed November 02, 2025)

[43] A. Almatroudi, Silver nanoparticles: synthesis, characterization, and biomedical applications. *Open Life Science*, 15 (2020) 1. pp. 819-839. https://doi.org/10.1515/biol-2020-0094. PMID: 33817269; PMCID: PMC7747521.

[44] C. Gibson, Investigating Initial Interactions between Silver Nanoparticles and Wastewater. Biological and Agricultural Engineering Undergraduate Honors Theses (2018). Retrieved from https://scholarworks.uark.edu/baeguht/47. (Accessed 02 November 2025)

JST&M 10(2026), 15 – 23
DOI: 10.57131/jstm.2026.10.2

Original scientific paper

HEALTH RISK ASSESSMENT OF HEAVY METALS IN THE LANDS AND PLANT CULTIVARS OF ZENICA MUNICIPALITY, BOSNIA AND HERZEGOVINA

Aida Šapčanin[1,2], Farzet Bikić[2], Muvedet Šišić[2], Vedran Stuhli[3]

[1]University of Sarajevo-Faculty of Pharmacy, [2]University of Zenica, Faculty of Engineering and Natural Sciences, [3]University of Tuzla, Faculty of Technology,

ABSTRACT

Estimating the risk to public health from heavy metals can help address basic questions about their potential dangers. This is the first study aimed to assess the health risk for the residents of the municipality of Zenica, on the land closest to the steel industry, by examining the heavy metals Zn, Ni, Pb, Cd, Cr, and Cu in the soil and plant cultivars corn and chard that could be used for the potential remediation of such soil. Using the calculated data for HQ and HI, the non-carcinogenic and carcinogenic risks for adults and children were estimated based on heavy metals in the selected topsoil and plants commonly grown in the area of interest, through different routes of intake. The results showed that there is an unacceptable risk for children and adults due to long-term consumption of investigated plant cultivars from soil contaminated with heavy metals. Constant monitoring and measures to reduce the heavy metal pollution, primarily Cd, Pb, and Cr, are necessary in the lands of the municipality of Zenica. Special caution is required for residents who intend to grow plant cultivars near the steel industry.

Keywords: Heavy metals, plant cultivars, soil, and health risk assessment.

Corresponding Author:
Aida Šapčanin
University of Sarajevo, Faculty of Pharmacy
Zmaja od Bosne 8, Sarajevo, Bosnia and Herzegovina
Tel.:
E-mail address: aida.sapcanin@ffsa.unsa.ba

1. INTRODUCTION

Risk analysis, as a paradigm, is science-based, problem-oriented, performed with fresh data, draws on information from different sources, makes the best decision at the most appropriate time, and produces flexible, up-to-date decisions. Risk assessment is a complex process for determining the risks related to some types of hazards in food - biological, chemical, or physical [1,2]. Risk characterization aims to assess the nature and likelihood of harm as a result of human exposure to various pollutants from plants and the land where they are grown [1,2]. Furthermore, it provides structured information that helps decision makers identify interventions that have public health significance and provides a basis for the use of various options. These options include regulatory measures when necessary. Risk assessment can also be used to identify collected data and target research that should increase the value of the assessment. In the future, risk assessment can help in the planning of science-based

remediation plans [3,4]. Namely, the basis that can be used for risk assessment helps in the identification of hazards whose occurrence is possible [2,5,6,7]. The real benefit is that the hazard is defined as the risk of negative health consequences, before it becomes contamination in the food chain [8]. With the introduction of risk analysis posed to heavy metals pollution worldwide, a new way of thinking about problems has been introduced. Many problems (e.g., food and environmental safety) still occurred and increased. The steel industry-associated activities, coal combustion, and intensive traffic in Zenica's municipality have become the main anthropogenic routes by which residents are exposed to elevated levels of toxic elements (such as Zn, Ni, Pb, Cd, Cr, and Cu) exceeding normal background levels [1,9,10]. Urban and agricultural lands are the major sink for these metals released into the environment, whereas they can negatively affect the chemical and biological soil quality [6,11,12,13]. Because of their potential toxicity, persistence, and bioaccumulation, elevated levels of these elements in the environment pose a serious threat to the public health of Zenica's population and cause serious concern, especially from malignant diseases [14,15,16]. Of particular concern is the increase in the number of patients and deaths from different kinds of cancer cause of heavy metal intoxications [17-20]. That is not surprising if it is known that in the winter months, a "cover" is formed over the small and narrow Zenica valley, under which all the toxic substances released from the chimneys and plants of the ironworks and other anthropogenic emissions remain as the toxic living atmosphere for the residents [11,15]. Many studies have confirmed similar health problems related to the toxic effects of heavy metals, especially in environments near various industrial plants, around the world [10,12,22,23,24]. The goal of this work was estimating the risk to adults and children health based on the content of heavy metals in the land of the potential agricultural area of the municipality of Zenica, where Zn, Ni Pb, Cd, Cr and Cu were identified as potential dangerous inorganic pollutants in the observed topsoil and plant cultivars, that are oftenly planted in this area and could serve for its potential phytoremediation.

2. EXPERIMENTAL PART

Topsoil and related plant cultivars (corn and chard) were collected and prepared from selected areas in the municipality of Zenica, near the steel company ArcelorMittal Zenica [2,25]. Specific locations (about 1000 m^2 each) for investigation were: Tetovo 44 13'52''N, 17 53'18''E, Podbriježje 44 21'17''N, 17 88'70''E, and Gradišće 44 24'04''N, 17 87'66''E, where the selected plants: corn and chard were cultivated. All samples were analyzed for the total content of the heavy metals by using an AAS method (Perkin Elmer spectrometer 3110), according to standard ISO 11466 and the Official Gazette of the Federation of Bosnia and Herzegovina [26]. In the accredited labs of the "Kemal Kapetanović" Institute, University of Zenica, all chemical analyses were performed.

a) Calculation of health risk assessment for soil:

The potential health risk assessment calculated for a lifetime of exposure (ingestion, inhalation, and dermal) based on USEPA model [27-32]., was determined as the cumulative carcinogenic and non - carcinogenic risk. The value of the total hazard index is calculated for the maximum content of heavy metals for adults and children. Non-carcinogenic and carcinogenic effects of heavy metals in soil were estimated by using equations:

$$ADDing = CM\ X\ \frac{IngR\ X\ EF\ X\ ED\ X\ CF}{BW\ X\ AT}$$

$$ADDinh = CM\ X\ \frac{InhR\ X\ EF\ X\ ED}{PEF\ X\ BW\ X\ AT}$$

$$ADDder = CM\ X\ \frac{SA\ X\ AF\ X\ ABS\ X\ EF\ X\ ED\ X\ CF}{BW\ X\ AT}$$

Where ADD_{ing} - Average daily doses (mg/kg day) via ingestion; ADD_{inh} - Average daily doses (mg/kg day) via inhalation, and ADD_{der} - Average daily doses (mg/kg day) via dermal contact.

Hazard identification basically aims to investigate pollutants that are present at any given location, their content, and spatial distribution. In the study area, Zn, Ni, Pb, Cd, Cr, and Cu were identified as possible hazards for the community. The non-carcinogenic effects of the elements were assessed by calculating the hazard coefficient and hazard index.

$$HQ = \frac{ADD}{RfD}$$

where HQ-hazard coefficient, RfD- Chronic reference dose (mg/kg day) of specific heavy metal, and HI-hazard index.

$$HI = \sum_{k=1}^{n} HQ_k = \sum_{k=1}^{n} \frac{ADD_k}{RfD_k}$$

The risk index (RI) predicts the potential cancer risk for children and adults in the study area by integrating all gathered information to produce quantitative estimates of cancer risk and hazard indices. Due to the lack of available values for slope factors (SF), we estimated carcinogenic risk only for exposure to Cd, Pb, and Cr, whose concentrations were the highest among the measured concentrations in the tested samples.

$$RI_{pathway} = \sum_{k=1}^{n} ADD_k\ CSF_k$$

where RI is unitless probability of an individual developing cancer over a lifetime; ADD_k is Average daily intake (mg/ kg day) for kth heavy metal, and CSF_k is Cancer slope factor (mg/ kg day)$^{-1}$ for kth heavy metal.

$$RI_{total} = RI_{ing} + RI_{inh} + RI_{der}$$

where RI_{ing}, $RI_{inh,}$ and RI_{der} are risk contributions through ingestion, inhalation, and dermal pathways.

The assessment is based on the following: If the elemental content of the metal is less than Rf, then HQ ≤ 1, which means that there are no adverse health effects. In the case that elemental content value is above Rf (HQ > 1), then adverse health effects are probable [28]. An HQ value higher than 10 indicates a high chronic risk for carcinogenic effects of the elements [22]. HI is the sum of all non-carcinogenic hazard quotients of the elements across all three exposure routes. If HI < 1, there is no risk of non-carcinogenic effects, while HI > 1 indicates a probability of adverse health effects. The RI is the probability that an individual will develop any type of cancer in their lifetime due to exposure to carcinogenic hazards. If the calculated RI < 10^{-6}, the carcinogenic health risk can be considered negligible. If the RI is in the range of 1×10^{-6} to 1×10^{-4}, then these values are within the acceptable risk to human health. If RI > 10^{-4}, then there is a high risk for developing cancer in humans.

b) Calculation of health risk assessment for plant cultivars consumption

To estimate the non-carcinogenic and carcinogenic health risk from consuming the plant cultivars (alfalfa, corn, and chard) contaminated with heavy metals, the target hazard quotient (THQ) was calculated as per the US EPA Region III Risk- Based Concentration Table. The THQ is calculated by the following equation:

$$THQ = \frac{EDI}{RfD}$$

where EDI is estimated daily intake; target hazard coefficient THQ is non-carcinogenic risk and is dimensionless; RfD is the reference dose of individual metal (mg/kg/ day).

Table 1. Parameters for health risk assessment of heavy metals in soil samples [27]

Factor	Definition	Unit	Value	
			Adults	Children
CM	Heavy metal content in soil or plants	mg/kg		
IngR	Ingestion rate of soil	mg/day	100	200
EF	Exposure frequency	days/year	350	350
ED	Exposure duration	years	30	6
BW	Body weight of the exposed individual	kg	70	15
AT	Average time	days	365ED	365ED
InhR	Inhalation rate of soil	m^3/day	20	10
PEF	Particle emission factor	m^3/day	$1.36x10^9$	$1.36x10^9$
SA	Exposed skin surface area	cm^2	5700	2800
AF	Skin adherence factor	mg/cm^2	0.07	0.2
CF	Calculation factor	kg/mg	10^{-6}	
ABF	Dermal absorption factor	none	0.1	0.1

Table 2. Reference doses and Cancer Slope factors for heavy metals [29]

Heavy metal	RfD_{ing} (mg/kg/dan)	RfD_{inh} (mg/kg/dan)	RfD_{der} (mg/kg/dan)	Oral CSF	Inhalation CSF
Zn	3.00×10^{-1}	3.00×10^{-1}	6.00×10^{-2}		
Ni	1.00×10^{-1}	2.00×10^{-3}	5.00×10^{-3}		8.40×10^{-1}
Pb	3.00×10^{-1}	3.00×10^{-3}	5.00×10^{-4}	8.50×10^{-3}	4.20×10^{-2}
Cd	1.00×10^{-3}	1.00×10^{-3}	$1.00x10^{-5}$	15	6.30
Cr	3.00×10^{-3}	2.00×10^{-4}	7.00×10^{-3}	5.00×10^{-1}	4.10×10^{1}
Cu	4.00×10^{-2}	4.00×10^{-1}	1.00×10^{-2}		

The reference oral dose (mg/kg/day) of selected metals is given in Table 2. To assess the overall potential health risk posed by different plant cultivars, the total hazard coefficient (TTHQ) was also calculated, where TTHQ <1 is safe, and TTHQ >1 is hazardous. To estimate the overall potential for non-carcinogenic health risk from all investigated heavy metals, HI can be calculated by the sum of the TTHQ metals of each plant cultivar [13]. Furthermore, carcinogenic risk (CR) was calculated using an equation:

$$CR = EDI\ X\ \ CSF\ oral$$

Generally, total CR values lower than 1 x 10^6 are considered to be minor, above 1 x 10^{-4} are unacceptable, and lying in the range of $1x10^{-6}$ to $1x10^{-4}$ is an acceptable range.

Quality control: The pre-cleaned tools, high-quality reagents, and standards were used, and three sample replicates were done during the AAS measurements of heavy metal content in topsoil and plant cultivars. Measured data for the total content of heavy metals were the subject of descriptive statistics. Relevant USEPA guidelines and ISO standards, and the environmental Bosnia and Herzegovina rulebook were used for performing the chemical analysis [26,33]. The calculations were done using Microsoft Excel software.

3. RESULTS AND DISCUSSION

Heavy metals topsoil analysis resulted in the following average data ranges (mg/kg): 30-100 for Zn, 40-120 for Ni, 20-70 for Pb, <1 for Cd, 30-180 for Cr and 20-40 for Cu. Generally, the results obtained from AAS measurements of selected heavy

metals indicated mild to moderate pollution of the investigated land area in Zenica. Enrichment factors (EF) were also calculated (as a ratio between the content of heavy metal in polluted soil and content of heavy metal in control soil), and obtained data were in the range: 0.7-1.3 for Zn, 0.8-3.6 for Ni, 0.7 -3.7 for Pb, 1 for Cd, 0.8 -1.4 for Cr, and 0.8 -1 for Cu. EF was calculated as a ratio to assess the pollution level of selected lands, where EF < 2 indicates anthropogenic non-harmful pollution, and EF 2-5 indicates moderate pollution. **T**he results showed the highest heavy metal pollution in the Gradišće area, in the following order: Ni > Pb > Zn > Cr > Cd > Cu. Similar results were obtained in other studies [1,9-11]. Furthermore, heavy metals analysis of selected plant cultivars resulted in the following average data ranges (mg/kg): 1-14 for Zn, 11-53 for Ni, 1-53 for Pb, 1-3 for Cd, 1-44 for Cr, and 1-39 for Cu. Regular monitoring of these lands is necessary in the goal of measuring the heavy metal content related to the soil matrix and possible enrichment caused by human activities and industrial emissions.

a) Soil non-carcinogenic and carcinogenic risk assessment

The values of average daily doses for adults and children are presented in Tables 3 and 4.

Due to soil exposure, the non-carcinogenic HQ and HI for adults and children were estimated using the 95th percentile value of the total metal concentration. The obtained results of the health risk of non-carcinogenic substances for adults and children, based on maximum metal concentrations in the tested soil and exposure through three different routes (ingestion, inhalation, and through the skin), are presented in Tables 5 and 6.

The data on risk pathway and total risk for adults and children are presented in Tables 7 and 8.

Potential carcinogenic risk will occur from Cr for children, as shown by the obtained results. Similar findings were obtained in foreign works where heavily polluted lands were investigated [13, 34].

b) Plants non-carcinogenic and carcinogenic risk assessment

The data of estimated daily intake, overall THQ, and HI for adults and children are presented in Tables 9 and 10

Results (Table 9) showed that the highest EDI contributions were of Pb and Cu from corn, especially for children.

This is in accordance with other similar investigations related to long-term consumption of cereals and vegetables cultivated in the polluted areas worldwide [3,6,13,35]. Corn is a plant cultivar with a very high bioaccumulation factor of investigated heavy metals [3, 36].

Table 3. Calculated values of ADD (mg/kg/day) of soil samples for adults

Heavy metals pathway	ADD (mg/kg/day)					
	Zn	Ni	Pb	Cd	Cr	Cu
ingestion	1.4×10^{-4}	1.7×10^{-4}	9.8×10^{-5}	1.4×10^{-6}	2.5×10^{-4}	5.6×10^{-5}
inhalation	2.8×10^{-8}	2.4×10^{-8}	1.4×10^{-8}	2×10^{-10}	3.6×10^{-8}	8×10^{-9}
dermal	3.3×10^{-5}	3.4×10^{-5}	2.3×10^{-5}	3.3×10^{-7}	5.9×10^{-5}	1.3×10^{-5}
total	3.4×10^{-3}	2×10^{-4}	1.2×10^{-4}	2.1×10^{-6}	3.1×10^{-4}	6.9×10^{-5}

Table 4. Calculated values ADD (mg/kg/day) of soil samples for children

Heavy metals pathway	ADD (mg/kg/day)					
	Zn	Ni	Pb	Cd	Cr	Cu
ingestion	6.4×10^{-4}	7.7×10^{-4}	4.5×10^{-4}	6.4×10^{-6}	3.1×10^{-3}	2.6×10^{-4}
inhalation	4.7×10^{-8}	5.6×10^{-8}	3.3×10^{-8}	4.7×10^{-10}	8.5×10^{-8}	1.9×10^{-8}
dermal	2.2×10^{-4}	2.6×10^{-4}	1.5×10^{-4}	2.2×10^{-6}	4×10^{-4}	8.8×10^{-5}
total	8.6×10^{-4}	1×10^{-3}	6.4×10^{-4}	8.6×10^{-6}	3.5×10^{-3}	3.5×10^{-4}

Table 5. Calculated HQ and HI values for adults

Different pathway	HQ					
	Zn	Ni	Pb	Cd	Cr	Cu
ingestion	4.7×10^{-4}	8.5×10^{-3}	2.7×10^{-2}	2.8×10^{-3}	8.3×10^{-2}	1.5×10^{-3}
inhalation	9.3×10^{-8}	1.2×10^{-5}	4.7×10^{-6}	3.5×10^{-6}	1.8×10^{-4}	-
dermal	4.4×10^{-4}	6.7×10^{-3}	4.6×10^{-2}	6.6×10^{-4}	8.4×10^{-3}	5.4×10^{-4}
HI	9.1×10^{-4}	1.5×10^{-2}	7.3×10^{-2}	3.5×10^{-3}	9.2×10^{-2}	2×10^{-3}

Table 6. Calculated HQ and HI values for children

Different pathway	HQ					
	Zn	Ni	Pb	Cd	Cr	Cu
ingestion	2×10^{-3}	3.9×10^{-2}	1.3×10^{-1}	1.3×10^{-2}	1	7×10^{-3}
inhalation	1.6×10^{-7}	2.8×10^{-5}	1.1×10^{-5}	8.2×10^{-6}	4.3×10^{-4}	-
dermal	2.9×10^{-3}	4.6×10^{-2}	3×10^{-1}	4.4×10^{-3}	5.7×10^{-2}	3.7×10^{-3}
HI	4.9×10^{-3}	8.5×10^{-2}	4.3×10^{-1}	1.7×10^{-2}	1.1	1.1×10^{-2}

Table 7. Calculated risk pathway and total risk for adults

Different pathway	Risk pathway		
	Pb	Cd	Cr
ingestion	8.3×10^{-7}	2.1×10^{-7}	1.3×10^{-6}
inhalation	5.9×10^{-10}	12.6×10^{-10}	1.5×10^{-8}
total tisk	8.3×10^{-7}	2.1×10^{-7}	1.3×10^{-6}

Table 8. Calculated Risk pathway and total risk for children

Different pathway	Risk pathway		
	Pb	Cd	Cr
ingestion	3.8×10^{-7}	9.6×10^{-5}	1.6×10^{-3}
inhalation	1.4×10^{-9}	2.9×10^{-9}	3.5×10^{-6}
Total Risk	3.8×10^{-7}	9.6×10^{-5}	1.6×10^{-3}

Table 9. Calculated EDI (mg/kg/day) for adults (a) and children (c)

Plant cultivar	EDI (mg/kg/day)											
	Zn		Ni		Pb		Cd		Cr		Cu	
	a	c	a	c	a	c	a	c	a	c	a	c
corn	0.001	0.007	0.020	0.096	0.032	0.152	0.002	0.010	0.010	0.048	0.031	0.147
chard	0.001	0.007	0.030	0.144	0.001	0.007	0.003	0.016	0.001	0.007	0.001	0.007

Table 10. THQ, TTHQ, and HI data for adults (a) and children (c)

Plant cultivar	THQ											
	Zn		Ni		Pb		Cd		Cr		Cu	
	a	c	a	c	a	c	a	c	a	c	a	c
corn	0.005	0.022	1.005	4.745	9.057	43.4	4.2	20.2	3.3	16	0.77	3.685
chard	0.005	0.022	1.505	7.205	0.400	1.91	6.6	31.2	0.47	2.2	0.035	0.168
TTHQ	0.010	0.044	2.510	11.950	9.457	45.31	10.8	51.4	3.77	18.2	0.805	3.853
HI adult	18.337											
HI children	42.705											

As the THQ data in Table 8 showed, potential non-carcinogenic risk posed to Cd, Pb, Cr, and Ni is seriously high for children as well as for adults for long-term consumption, especially of corn in the investigated lands. Similar results for the highest values of THQ and HI were found in the papers about health risk assessment of soil and edible plants in different countries, especially in areas near heavy industries - steel, petrochemical, etc. [5,6, 13,34].

The data of CR and total CR for adults and children are presented in Table 11.

Table 11. CR and total CR data for adults (a) and children (c)

Plant cultivar	CR					
	Cd		Pb		Cr	
	a	c	a	c	a	c
corn	3.2×10^{-2}	1.5×10^{-3}	2.7×10^{-4}	1.3×10^{-3}	5×10^{-3}	2.4×10^{-2}
chard	5×10^{-2}	2.3×10^{-3}	2×10^{-5}	5.7×10^{-5}	7×10^{-4}	3.4×10^{-3}
Total CR	8.2×10^{-2}	3.8×10^{-3}	2.9×10^{-4}	1.3×10^{-3}	5.7×10^{-3}	2.7×10^{-2}

Results showed that the potential carcinogenic risk calculated for target metals such as Cd, Pb, and Cr is unacceptable for children as well as for adults in the municipality of Zenica, as the CR values were above the safe limit of 10^{-4}.

4. CONCLUSIONS

Our study assessed both non-carcinogenic and carcinogenic health risk due to exposure to heavy metals Zn, Ni, Pb, Cd, Cr, and Cu through the soil - plant human contamination pathway next to the typical steel industry in the area of the municipality of Zenica. The soil was polluted with different metals, which was shown by the results of the chemical analysis of the selected metals and the calculated EF data. Particularly worrisome data were obtained for Cd, Ni, Pb, and Cr after the evaluation of the health risk for the soil and the tested plant cultivars through different routes of intake of these heavy metals. Our study could serve as a model for similar estimations that would deal with public health risk assessment in areas that are particularly contaminated by known industrial emitters.

Acknowledgements

This work was supported by the Federal Bosnia and Herzegovina Environmental Protection Fund and was carried out within the framework of the project „Study of the effect of chelate addition to the phytoremediation potential of plants at soils contaminated with heavy metals" (Grant no. 01-09-2-3535/2024, dated 16.07.2024).

Conflict of Interest

The authors declare no conflict of interest.

5. REFERENCES

[1] S. Murtić, J. Jurković, E. Bašić, E. Hekić, Assessment of wild plants for

phytoremediation of heavy metals in soils surrounding the thermal power station, *Agronomy Research*, 17 (2019) 1, pp. 234- 244

[2] A. Šapčanin, E. Pehlić, S. Korać, E. Ramić, B. Pehlivanović, Consumption of cereals in Bosnia and Herzegovina - the health risk calculation. In: New Technologies, Development and Application IV, NT 2021. Lecture Notes in Networks and Systems, Isak Karabegović Eds., Springer Nature: Switzerland 472, 2022, pp. 823-829

[3] O. T. Aladesanmi, J. G. Oroboade, C. P. Osisiogu, A. O. Osewole, Bioaccumulation factor of selected heavy metals in *Zea mays*. *Journal of Health & Pollution*, 9 (2019) 24, pp. 2-19

[4] A. K. Priya, M. Muruganandam, S. S. Ali, M. Kornaros, Cleanup of Heavy Metals from Contaminated Soil by Phytoremediation: A Multidisciplinary and Eco-Friendly Approach, *Toxics*, 11 (2023) 5, pp. 422-446

[5] L. Cao, C. Lin, C. Sun, L. Xu, L. Zheng, Health risk assessment of trace elements exposure through the soil-plant (maize)-human contamination pathway near a petrochemical industry complex, Northeast China, *Environmental Pollution*, [Online], 263 (2020), 114414

[6] A. Adam, L. N. Sackey, L. A. Ofori, Risk assessment of heavy metals concentration in cereals and legumes sold in the Tamale Aboabo market, Ghana, *Heliyon*, [Online], 8 (2022), 10162

[7] V. Antunović, D. Blagojević, R. Baošić, D. Relić, A. Lolić, Health risk assessment of heavy metals in soil, plant, and water samples near "Gacko" power plant, in Bosnia and Herzegovina, *Environ Monit Asses,* 195 (2023), pp. 596-605

[8] B. R. Shetty, P. B. Jagadeesha, S. A. Salmataj, Heavy metal contamination and its impact on the food chain: exposure, bioaccumulation, and risk assessment. *CyTA - Journal of Food*, [Online], 23 (2025) 1, 2438726

[9] J. Alijagić, R. Šajn, Distribution of chemical elements in an old metallurgical area, Zenica (Bosnia and Herzegovina). *Geoderma,* 162 (2011) 1-2, pp. 71- 85

[10] S. Beganović, H. Prcanović, M. Duraković, A. Adrović, Heavy metal bioaccumulation in Zea Mays L. I Medicago Sativa L. in the area of Zenica, *International Journal of Advanced Research (IJAR)*, 13 (2025) 3, pp. 112-119

[11] M. Duraković, A. Husika, H.S. Prcanović, S. Beganović., M. Šišić, Environmental burden by total sediment dust in the city of Zenica, *International Journal of Advanced Research (IJAR)*, 10 (2022) 11, pp. 125-132

[12] A. Ene, A. Sion, C. Stihi, A. I. Gheboianu, V. Basliu, A. M. Ceoromila, S. Gosav, Metal Contamination and Human Health Risk Assessment of Soils from Parks of Industrialized Town (Galati, Romania). *Applied Sciences,* [Online], 14 (2024), 10379

[13] A. I. Chowhudury, L. C. Shill, M. M. Raihan, R. Rashid, N. H. Bhuiyan, S. Reza, M. R. Alam, Human health risk assessment of heavy metals in vegetables of Bangladesh. *Scientific Reports*, [Online], 14 (2024), pp. 5616-5632

[14] S. Durmišević, S. Kubat, J. Durmišević Serdarević, M. Lelić, Air pollution effect on the malignant disease mortality rate in the city of Zenica, In: 17th International Research/Expert Conference-TMT: proceedings, Istanbul, Turkey, 2013, pp. 285-288

[15] H. Hodžić, M. Bazardžanović, S. Jagodić, M. Hiroš, M. Kulovac, M. Oruč, M. Mahmić-Kaknjo, Clinical importance of dependent prognostic factors for renal parenchymal carcinoma and possibility of predicting the treatment outcome, *Med Glasnik*, 11 (2014) 1, pp. 145-151

[16] S. Sivić, Mortality associated with seasonal changes in ambient temperature and humidity in Zenica-Doboj Canton, *Med Glasnik*, 18(2021) 2, pp. 516-521

[17] M. Radfard, H. Hashemi, M. A. Baghapour, M.R. Samaei, M. Yunesian, H. Soleimani, A. Azhadarpoor, Prediction of human health risk and disability-adjusted life years induced by heavy metals exposure through drinking water in Fars Province, Iran, *Scientific Reports*, [Online], 13 (2023), 19080

[18] D. Caradduzza, A. Congiargiu, E. Azara, I. M. A. Mamani, M. De Miglio, A. Zinellu, C. Carru, S. Medici, Heavy metals in biological samples of cancer patients: a systematic literature review, *BioMetals*, [Online], 37 (2024), pp. 803-817

[19] A. H. Khoshakhlagh, M. Mohammadzadeh, A. Gruszecka-Kosowska, The preventive and carcinogenic effect of metals on cancer: a systematic review, BMC *Public Health*, [Online], 24, (2024), 2079

[20] M. M. Tomlison, F. Pugh, A. N. Nail, K. Udoh, S. Abraham, S. Kavalukas, B. Guinn, R. M.

Tamimi, F. Laden, H. S. Iyer, J. C. States, M. Ruther, C. T., Ellis, N. DuPre, Heavy−metal associated breast cancer and colorectal hot spots and their demographic and socioeconomic characteristics. *Cancer Causes and Control*, [Online], 35 (2024), pp. 1367-1381

[21] X. Qing, Z. Zutong, L. Shenggagao, Assessment of heavy metal pollution and human health risk in urban soils of steel industrial city (Anshan), Liaoning, Northeast China, *Ecotoxicology and Environmental Safety*, [Online], 120 (2015), 377-385

[22] S. Salmani-Ghabeshi, M. R. Palomo-Marin, E. Bernalte, F. Rueda-Holgado, C. MiroRodriguez, F. Cereceda-Balic, X. Fadic, V. Vidal, M. Funes, E. Pinilla-Gil, Spatial gradient of human health risk from exposure to trace elements and radioactive pollutants in soils at the Puchuncavi-Ventanas industrial complex, Chile. *Environ. Pollut.*, [Online], 218 (2016), pp. 322–330

[23] A. Kharazi, M. Leili, M. Khazaei, M. Z. Alikhani, Human health risk assessment of heavy metals in agricultural soil and food crops in Hamadan, Iran, *Journal of Food Composition and Analysis*, [Online], 100 (2021), 103890

[24] M. Šljivić Husejnović, S. Janković, D. Nikolić, B. Antonijević, Human health risk assessment of lead, cadmium, and mercury co-exposure from agricultural soils, *Arhiv za higijenu rada i toksikologiju*, 72 (2021) 4, pp. 268-279

[25] A, Šapčanin, E. Pehlić, S. Korać, E. Ramić, B. Pehlivanović, Estimating the health risk of heavy metals in edible plants to the general population in Sarajevo, B&H, In New Technologies, Development and Application IV. NT 2021. Lecture Notes in Networks and Systems, Isak Karabegović Eds., Springer Nature: Switzerland, 233, 2021, pp. 883-889

[26] Pravilnik o utvrđivanju dozvoljenih količina štetnih i opasnih materija u tlu Federacije Bosne i Hercegovine i metodama njihovog ispitivanja, Službene novine Federacije Bosne i Hercegovine, Sarajevo: Federacija Bosne i Hercegovine; 2009, broj 72/09.

[27] WHO, World Health Organization, Environmental Health Criteria Series, EHC 228. Principles and Methods for the Assessment of Risk from Essential Trace Elements. WHO Geneva, 2002

[28] USEPA, Supplemental Guidance for Developing Soil Screening Levels for Superfund Sites, OSWER 9355.4-24, Office of Solid Waste and Emergency Response, 2001

[29] US EPA, A review of the reference dose and reference concentration processes. EPA/630/P-02, 2002

[30] USEPA, Risk Assessment Guidance for Superfund Volume I: Human Health Evaluation Manual (Part A). Office of Emergency and Remedial Response, Washington, DC. 2004

[31] US EPA, United States Environmental Protection Agency, in Quantitative Risk Assessment Calculations 7−9, 2015

[32] [32] USEPA US Environmental Protection Agency, Resident Soil Table, 2017.

[33] International Standard Office ISO 11466: 1996, Soil quality −Extraction of trace elements soluble in aqua regia, 2016

[34] X. Xiao, J. Zhang, H. Wang, X. Han, J. Ma, Y. Ma, H. Luan, Distribution and health risk assessment of potentially toxic elements in soil around coal industrial areas: a global meta-analysis. *Sci. Total Environ*, [Online], 713 (2020), 135292

[35] A. Wodkowska, A. Gruszecka-Kosowska, Dietary exposure to potentially harmful elements in edible plants in Poland and the health risk dynamics related to their geochemical differentiation, *Scientific Reports*, [Online], 13 (2023), 8521

[36] C. Rubio-Armendariz, S. Paz, A. J, Gutierrez, D. Gonzales-Weller, C. Revert, A. Hardisson, Human exposure to toxic metals (Al, Cd, Cr, Ni, Pb, Sr) from the consumption of cereals in Canary Islands, *Foods*, [Online], 10 (2021) 6, 1158

JST&M 10(2026), 24 – 29
DOI: 10.57131/jstm.2026.10.3

Original scientific paper

STABILIZATION OF RED MUD WITH NATURAL MINERALS

Edina Ibrić[1], Vedran Stuhli[1], Enita Kurtanović[2], Mugdin Imamović[3]

[1]Faculty of Technology, University of Tuzla, [2]AD HARBI d.o.o., Sarajevo, [3] Lukavac Cement d.o.o., Lukavac

ABSTRACT

This work aimed to examine the possibility of stabilizing red mud with a natural mineral, namely pyrophyllite shale, to the extent that it is not harmful to the environment, as well as the use of such a stabilized composite for the production of building materials such as bricks, to ultimately achieve a complete circular economy, where, on the one hand, there would be the utilization of waste material, the preservation of the environment and natural resources, and, on the other hand, the production of products of the same quality. Based on the set goal, the results for the composition of red mud and pyrophyllite shale, as well as the stabilized composite before and after thermal treatment at 900 °C, are presented in the work, and they show that there is a decrease in the proportion of all oxides present in the mixture except silicon, because it is over 63% in pyrophyllite shale. Based on the stabilized composite, building block samples were formed. After the firing process, the samples cracked, and as such, they could not be analyzed further. Based on this, it could be concluded that only the stabilized composite cannot be used to make bricks.

Keywords: red mud; pyrophyllite shale; stabilization; composite; building block

Corresponding Author:
Edina Ibrić,
Faculty of Technology, University of Tuzla
Urfeta Vejzagića 8, 75000 Tuzla, BiH
Tel.: 060 321 7221
E-mail address: edina.ibric@untz.ba

1. INTRODUCTION

1.1. Red mud

Bauxite residue, or red mud, is a solid waste product resulting from the processing of bauxite ore into alumina. Red mud is mainly collected from the Bayer process, which uses sodium hydroxide to dissolve aluminum silicates. Approximately 35–40% of the processed bauxite ore is discarded as alkaline red mud, which consists of 15–40% solids, and 1 to 1.5 t of red mud is left over from the production of 1 t of alumina [1]. As a solid waste, red mud is usually disposed of in sludge ponds as sludge deposits or in ponds as dry sludge near alumina production plants, or it is directly discharged through pipelines into the nearby sea. Due to its fine particle characteristics, high alkalinity (pH 10–12.5), and metal content, the disposal of large quantities of red mud has caused serious environmental problems, including soil pollution, groundwater pollution, and marine fine particle suspension. The storage of red mud in lakes or ponds takes up huge areas, and the storage of dry red

mud can also lead to dust pollution, which is a serious health problem for people living near red mud dumps, because breathing brings in small particles that accumulate in the body, and they have a very bad effect on human health. The cost of red mud disposal is relatively high and accounts for about 2% of the cost of alumina [2].

On the other hand, red mud consists of valuable materials such as rare earth elements, titanium, iron, and aluminum. Typical amounts of Ti, Si, Fe, Na, and Al in red mud are 2–12%, 1–9%, 14–45%, 1–6%, and 5–14%, respectively [3]. However, despite the invaluable results obtained from research related to the use of red mud, they are not practically applicable for recycling large quantities of red mud (i.e., currently 150 million tons per year [3,4]). Of all the elements present in red sludge, iron occupies the largest share in the form of oxides or hydroxides, and by disposing of and not using red sludge, large amounts of iron are also disposed of, approximately 20 Mt per year [5].

1.2. Pyrophyllite schist

Pyrophyllite schist is a hydrated aluminum silicate with the chemical formula $Al_2Si_4O_{10}(OH)_2$ and is commonly associated with other minerals such as quartz, mica, kaolinite, epidote, and rutile. Pure pyrophyllite shale consists of 28.3% Al_2O_3, 66.7% SiO_2, and 5% H_2O by mass. Pyrophyllite shale, when pure, is desirable for many applications because of its unique properties. For example, pyrophyllite provides low thermal and electrical conductivity; high refractive behavior; low coefficient of expansion; high corrosion resistance; low bulk density; and low hot load deformation. Therefore, this mineral is widely used in the refractory, ceramic, and pharmaceutical industries, but also in the production of pesticides, fertilizers, paper, paints, plastics, rubber, cement, etc. [6]

1.3. Building block

Building materials are understood as natural or artificial materials, which are used in the form of raw materials, semi-finished products, or finished products for the construction of buildings. In addition to the binding layer, the essential construction material is a building block, as a unit element for masonry, with dimensions and mass adapted to the handling of workers; most often in the form of a cube, with or without cavities. The simplest building block is essentially a traditional material called brick. The term brick refers to small units of building material, often made of baked clay and attached with mortar, a binding agent consisting of cement, sand, and water.

Today, bricks are produced from brick clay or loam with additives. Clay is the basic plastic raw material. The most common additives can be stone sand, limestone or marl clay, and iron hydroxide. Clays with a large number of impurities absorb water poorly, which is one of the disadvantages. The basic property of clay is its plasticity. This allows it, when mixed with water, to produce a dough that does not crack or tear during shaping, while retaining its shape after drying and baking. The brick production process begins with the mixing and grinding of raw materials in mills. After grinding in coarse mills, scattering, aging, and homogenization are carried out in rooms with sufficient moisture. After that, the clay is ground again in fine mills, and its shaping is carried out in a vacuum press [7].

2. EXPERIMENTAL RESEARCH

The experimental plan was to investigate the possibility of using pyrophyllite shale, as a natural mineral, to stabilize red mud to a form that is not harmful to the environment, as well as the use of such a formed composite for the production of building blocks or bricks. A mass ratio of 1:1, 1:2, and 1:3 was used to form the composite of red mud and pyrophyllite shale. Before forming the building block

samples, with the specified proportions of red mud and pyrophyllite, it was first necessary to convert the components into the same shape, so a ball mill was used for this. The samples were formed in a mold measuring 4x4x20 (cm) under the same conditions. The specified dimensions for forming the building block represent standard dimensions for subsequent analyses of the finished samples for further testing. After mixing the composite with water and filling the molds, the samples were air-dried for three days at room temperature to release moisture, leading to a volume decrease. The drying continued in an oven at 105 °C for 32 hours before firing in an annealing oven, which included an initial half-hour at 550 °C to evaporate residual moisture and prevent cracking, followed by a two-hour duration at 900 °C, and concluded with a cooling phase before the final samples were removed. The finished samples are shown in Figure 1.

Figure 1. Finished samples of the building block

3. RESEARCH RESULTS WITH DISCUSSION

In order to determine the success of the stabilization of red mud with pyrophyllite shale, the composition of red mud, pyrophyllite shale, and the formed composite was analyzed before and after thermal treatment at 900 °C, while the formed building block samples were subjected to analysis to determine the compressive strength. The pH value of the red mud was in the alkaline range, as in the case of pyrophyllite shale, but with pronounced buffer properties. The forms of metal elements in a stable state with lower mobility and reactivity in the alkaline range were recorded. In the next step of the experiment, when the composite was subjected to the firing temperatures of the building block, the conversion of the present metal components into an inert oxide form was performed. The composition of the components used in the oxide form is shown in Tables 1 and 2.

Table 1. Analysis of the composition of pyrophyllite schist

Oxide	mas.%
SiO_2	63.08
Al_2O_3	27.42
CaO	4.44
Fe_2O_3	1.54
K_2O	1.24
MgO	0.79
Na_2O	0.63
TiO_2	0.27
ZnO	0.05

Table 2. Analysis of the composition of red mud

Oxide	mas.%
Fe_2O_3	43.93
Al_2O_3	17.91
SiO_2	6.79
TiO_2	10.2
Na_2O	6.9
CaO	8.96

For the sake of easier comparison, Figure 2 shows the composition of red mud and pyrophyllite slate, where it can be seen that in the pyrophyllite slate, the oxides SiO_2 and Al_2O_3 are present in the largest proportion, while in the red mud, Fe_2O_3, Al_2O_3, SiO_2, and TiO2 are present, while the remaining oxides are present in smaller, negligible amounts.

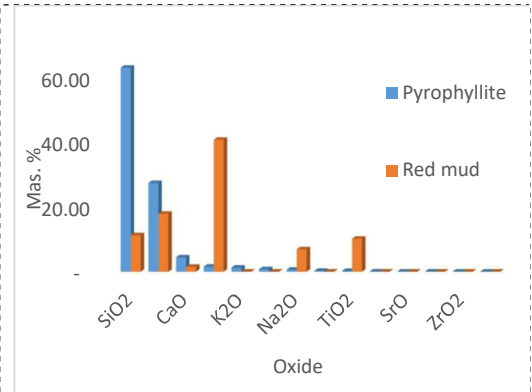

Figure 2. Graphic representation of the presence of metals in red mud and pyrophyllite shale

In Table 3, the composition of the formed composite is shown for three samples, i.e., three different ratios of pyrophyllite and red mud (Sample A 1:1, Sample B 1:2, Sample C 1:3). Of all the oxides in the analysis, only SiO_2 shows a trend of increasing concentrations (28.58 – 35.6 – 41.69 %) with an increase in the proportion of the pyrophyllite component, which is logical because pyrophyllite shale has 66.7 % SiO_2 in its composition. Other oxides generally decrease, indicating selective dilution and chemical inertness of certain components such as Al_2O_3 (25.99 – 20.05 – 24.11 %).

Table 3. Analysis of the composition of pyrophyllite schist

Oxide	Unit	Sample A	Sample B	Sample C
SiO_2	%	28.58	35.6	41.69
Fe_2O_3	%	25.99	20.05	16.93
Al_2O_3	%	23.36	24.97	24.11
CaO	%	13.05	11.43	10.22
TiO_2	%	4.05	3.31	2.8
Na_2O	%	2.8	2.48	2.15
MgO	%	0.59	0.56	0.62
SiO_2	%	28.58	35.6	41.69

Figures 3, 4, and 5 show XRD analysis of the mineralogical composition for samples A, B, and C, or XRD diffractograms, before and after heat treatment, with visible results, which reflect the change in the mineralogical proportion of individual components.

In all three ratios of the composite, the samples before firing have more intense peaks; they indicate a better arrangement of the crystalline state and more crystalline substances, unlike the sample that was fired at 900 °C. This relationship is recorded in the range of values of the angle 2Θ = 0 – 33. Beyond this value, the heat-treated sample exhibits crystallinity. Better ordering of the crystalline state can be traced up to the value of the angle 2Θ = 36, after which it significantly decreases (individual peaks of lower intensity appear). That means the crystalline state is correlated with the increase of the pyrophyllite component in the composite. In addition to examining the composition of red mud and pyrophyllite shale before and after stabilization, the formed building blocks were to be subjected to several analyses, such as compressive strength and water absorption properties, etc.

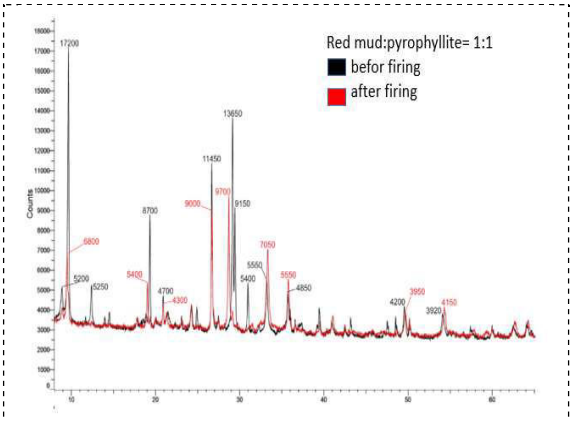

Figure 3. XRD diffractogram for sample A

However, this was not possible because the samples, after finishing the baking process, had already cracked and, as such, could not be used for further analysis.

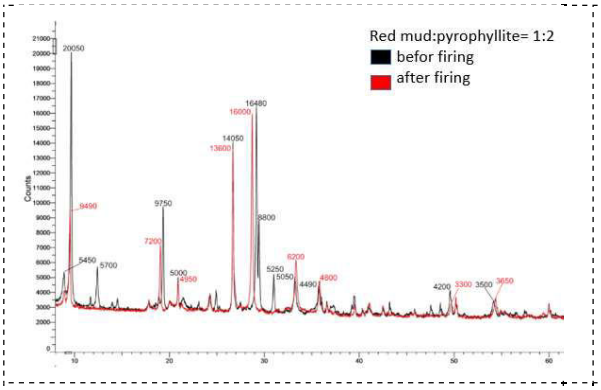

Figure 4. XRD diffractogram for sample B

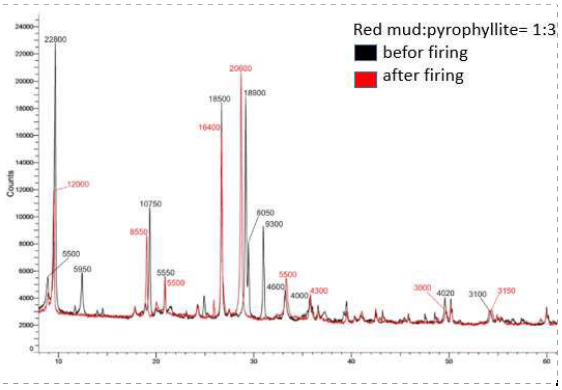

Figure 5. XRD diffractogram for sample C

Several mechanisms can explain the observed stabilization. First, the high SiO_2 and Al_2O_3 contents of pyrophyllite promote the formation of a more stable silicate matrix that can accommodate reactive components of red mud, thereby reducing their leaching. Aluminosilicate minerals have been shown to immobilize heavy metals and to stabilize alkaline wastes [2,4]. Moreover, the pre-fired composites exhibit a much higher degree of crystallinity in XRD analysis, indicating a more ordered arrangement that contributes to initial structural stability. During firing, some peaks diminish in intensity, which probably corresponds to phase transformations and partial melting, which affects the structural integrity.

The fractured fired building blocks are due to the mismatch in thermal expansion as well as the high content of Fe_2O_3 from red mud. During firing, iron oxides serve as fluxes and lead to a decrease in the softening point and internal stresses due to different expansion rates and phases. Industrial wastes are a potential medium of high-iron loading that will have to be blended with plastic clays to obtain solid bricks, since iron-contaminated waste might contribute towards thermal stress on the brick of the same type [1,7]. Thus, while the solidified red mud–pyrophyllite composite provides some protection for hazardous materials, it has limited capability of making crack-free bricks by itself. One potential strategy is to utilize the stabilized mixtures as an additive to traditional clay blending to enhance environmental safety without compromising mechanical integrity. These results add to the literature by showing the chemical stabilization of red mud with pyrophyllite, but not to new brick processes directly.

Contrary to other literature work, which works with red mud mostly for soil or pigment stabilization, this work focuses on combining stabilization mechanisms with circular economy strategies and proposes the possibility of valorization of industrial waste materials while preserving building materials' performance.

4. CONCLUSIONS

To determine the success of the stabilization of red mud with pyrophyllite shale, an analysis of the composition of red mud, pyrophyllite shale, and the formed composite was performed before and after thermal treatment at 900 °C. The composition analysis shows that pyrophyllite shale consists mainly of oxides SiO_2 (63.08%) and Al_2O_3 (27.42%), and red mud consists of Fe_2O_3 (43.93%), Al_2O_3 (17.91%), SiO_2 (6.79%), and TiO_2 (10.2%), while other oxides are present in smaller, negligible amounts.

Analysis of the composition of the formed composite for all three samples, i.e., three different ratios of pyrophyllite shale and red mud (Sample A 1:1, Sample B 1:2, Sample C 1:3), indicates that of all the oxides present, only SiO_2 records a trend of increasing concentrations (28.58 – 35.6 – 41.69%) with an increase in the share of the pyrophyllite component, which is logical because pyrophyllite shale in its composition has 63.08% SiO_2. The content of Al_2O_3 (25.99 – 20.05 – 24.11%) is quite uniform, which can be explained by its inertness, while a decrease in concentrations was recorded for other oxides.

XRD analysis of the formed composite shows that for all three composite ratios, the samples before firing have more intense peaks, which indicates a better order of the crystalline state, more crystalline substances, unlike the sample fired at 900 °C. This relationship is recorded in the range of values of the angle $2\Theta = 0 - 33$. Beyond this value, the heat-treated sample exhibits crystallinity.

The initial experiment to create building blocks using red mud and pyrophyllite slate was unsuccessful because the samples cracked after firing, indicating that the proportions used were unsuitable.

However, the successful stabilization of red mud with pyrophyllite suggests a potential alternative application, warranting further research into using the stabilized mud as an additive to clay for brick production.

Conflict of Interest

The authors declare no conflict of interest.

5. REFERENCES

[1] L. Zhan, Production of bricks from waste materials, *Constr. Build. Mater.*, [Online], 47 (2013), pp. 643–655.

[2] V. Feigl, A. Anton, N. Uzigner, K. Gruiz, Red mud as a chemical stabilizer for soil contaminated with toxic metals, *Water Air Soil Pollut*, [online], 223 (2012), pp.1237–1247

[3] W. Huang, S. Wang, Z. Zhu, L. Li, X. Yao, V. Rudolph, F. Haghseresht, Phosphate removal from wastewater using red mud, *Journal of Hazardous Materials,* 158 (2008) 158, pp.35-42

[4] Sushil, V. Batra, Catalytic applications of red mud, an aluminium industry waste: A review, *Applied Catalysis B: Environmental*, 81 (2008), 1-2, pp. 64-77

[5] J. Mikić, D. Lazić, J. Pwnavin-Škundrić, M. Prtušić, D. Kešelj, D. Blagojević, G. Ostojić, Crveni mulj kao pigment u proizvodnji betonskih elemenata, *Reciklaža i održivi razvoj*, 6 (2013) 1, pp. 18-25

[6] T. Mukhopadhyay, S. Ghatak, H. Maiti, Pyrophyllite as raw material for ceramic applications from the perspective of its pyro-chemical properties, Ceram. Int., 36 (2010) 3, pp. 909–916

[7] W. Bender, F. Handle, *Brick and Tile Making*, Bauverlag GmbH, 1985

JST&M 10(2026), 30 – 35
DOI: 10.57131/jstm.2026.10.4

Original scientific papers

ELECTROCHEMICAL INFLUENCE OF NIFUROXAZIDE ON DEHYDROGENASE ACTIVITY

Safija Herenda[1], Nenad Vanis[2], Farzet Bikić[3], Edhem Hasković[4]

[1]Department of Chemistry, Faculty of Science, University of Sarajevo, [2]Asa Hospital, Sarajevo, [3]Faculty of Engineering and Natural Sciences, University of Zenica, [4]Department of Biology, Faculty of Science, University of Sarajevo

ABSTRACT

Nifuroxazide is an antimicrobial drug from the nitrofuran group, which is used in the treatment of acute bacterial intestinal infections. Its mechanism of action is based on the reduction of the nitro group in bacterial cells, which produces reactive metabolites that permanently damage enzymes and the genetic material of microorganisms. Enzymes of redox metabolism are particularly sensitive, among which lactate dehydrogenase (LDH) stands out. In this work, an electrochemical method (cyclic voltammetry and chronoamperometry) was used to determine kinetic constants. The enzyme LDH (biosensor) was immobilized on a GC electrode, and the effect of nifuroxazide on enzyme activity was monitored. The results show that nifuroxazide binds non-competitively to the enzyme and thus changes the enzyme conformation. This process leads to permanent blockade of key metabolic reactions, disruption of the redox balance, and death of the bacterial cell.

Keywords: biosensors; enzyme; electrochemical method; kinetics;

Corresponding Author:
Safija Herenda
Department of Chemistry, Faculty of Science, University of Sarajevo
Zmaja od Bosne 33-35, Sarajevo 71000, Bosnia and Herzegovina
Tel.: +0-000-000-0000 ; fax: +0-000-000-0000 .
E-mail address: safija@pmf.unsa.ba

1. INTRODUCTION

Nifuroxazide is a nitrofuran derivative, containing a nitro group that can participate in redox reactions. It acts on bacterial enzymes involved in protein synthesis and metabolism, especially those that depend on oxidoreductase processes. The nitro group can be reduced in bacterial cells, creating reactive intermediates that damage enzymes and DNA. This leads to inhibition of bacterial and parasitic growth. Nifuroxazide is a selective inhibitor of bacterial oxidoreductases, and its reactive metabolites secondarily block dehydrogenases, transaminases, and DNA replication enzymes. This achieves a combined effect: blockade of energy metabolism, protein synthesis, and damage to genetic material, which leads to the death of the bacterial cell. The role of dehydrogenases (E.g., Lactate dehydrogenase) is crucial in energy metabolism, and their sensitivity stems from the fact that reactive metabolites of nifuroxazide interfere with electron transfer in these enzymes. The consequence of inhibition is a disruption in the formation of ATP and the energy balance of bacteria. Lactate dehydrogenase inhibitors are

commonly investigated chemical compounds for the treatment of cancer. Most cancer cells switch their metabolism from mitochondrial oxidative phosphorylation to aerobic glycolysis to generate ATP and precursors for the biosynthesis of key macromolecules. Aerobic conversion of pyruvate to lactate, coupled with oxidation of the nicotinamide cofactor, is a primary hallmark of cancer and is catalyzed by lactate dehydrogenase (LDH), the central effector of this pathological reprogrammed metabolism. Therefore, inhibition of LDH is a potential new, promising therapeutic approach for the treatment of this severe, currently incurable disease [1]. The nitro group of nifuroxazide is electrochemically active and undergoes reduction in bacterial cells.

It creates toxic intermediates that interfere with enzymes dependent on oxidoreductive reactions. The mechanism of action of nifuroxazide consists of several steps. The first step is entry into the bacterial cell, where it reaches the intestinal lumen and contacts bacteria, is not absorbed systemically, and acts locally. Then, the nitro group is reduced because bacterial oxidoreductases reduce the nitro group of nifuroxazide, and reactive intermediates (radicals, aldehydes) are formed. The third step in the mechanism is the formation of toxic metabolites that bind to the sulfhydryl groups of enzymes and damage key metabolic enzymes (dehydrogenases, transaminases). Inhibition of protein synthesis and energy metabolism is the fourth step, where the blockade of enzymes leads to disruption of protein synthesis, and energy cycles (ATP production) are interrupted. Then follows DNA damage, reactive metabolites attack DNA, while DNA replication and repair enzymes are inhibited. The final step in the mechanism is the death of the bacterial cell, where a combination of enzyme blockade and DNA damage leads to a bactericidal effect. Enzyme inhibitors currently represent almost half of the drugs in clinical use; therefore, selective inhibition of enzymes of infectious organisms (e.g., viruses, bacteria, and multicellular parasites) is an attractive means of chemotherapeutic intervention for infectious diseases. This strategy is well represented in modern medicine, and a significant part of antiviral, antibiotic, and antiparasitic drugs in clinical use today derive their therapeutic efficacy from the inhibition of selective enzymes [2]. In this work, an electrochemical method was used to study the influence and inhibitory properties of nifuroxazide on the activity of the enzyme lactate dehydrogenase (LDH). Direct electrochemistry of the enzyme can provide a good model for investigating enzymatic activity and electron transfer in biological systems [3]. This work aims to determine the binding mode of nifuroxazide by the electrochemical method, determine the type of inhibition, and the kinetic constants.

2. EXPERIMENTAL

Materials: Lactate dehydrogenase enzyme LDH Assay Kit AB102526 Abcam (Cambridge); KH_2PO_4 and Na_2HPO_4, Fisher Chemical (Wien, Austria); Nafion Sigma-Aldrich (Buchs, Switzerland); Nifuroxazid, Bosnalijek, BiH.

Methods: The instrument used for the measurements was a potentiostat/galvanostat Vertex one, Ivium Technologies, with a classic three-electrode system in which a saturated Ag/AgCl electrode was used as a reference electrode, a Pt electrode as a counter electrode, and GC (glassy carbon) as a working electrode. An amperometric biosensor was formed by immobilizing an enzyme (LDH) trapped in a Nafion layer on the surface of the GC electrode, as described in the literature [4,5]. The electrochemical methods used for the measurements were cyclic voltammetry and chronoamperometry.

Cyclic voltammetry was used to investigate the immobilization of the enzyme film on the electrode surface. All cyclic voltammetry tests were performed in physiological phosphate buffer solution (pH 7) and in the potential range from -1.0 to 1.0

V, at a scan rate of 50 mV/s. Chronoamperometric technique was used to determine kinetic parameters: Michaelis-Menten constant (K_m) and the maximum current value when the solution is saturated with substrate (I_{max}), which is equivalent to the maximum reaction rate (V_{max}), as well as to determine the type of inhibition [6]. Chronoamperometric measurements were performed in a 25 mL phosphate buffer cell at a constant potential of 0.9 V imposed on the working electrode, as well as at constant stirring of 400 rpm. The reaction was observed in the absence and presence of different concentrations of nifuroxazide.

3. RESULTS AND DISCUSSION

In an enzyme sensor, the signals generated by enzymatic reactions are converted into electrical signals by a GC electrode [7,8]. The immobilized enzyme exhibits good sensitivity, selectivity, and response time. Many types of dehydrogenases catalytically transport electrons to their respective electron acceptors. The kinetic parameters obtained by the analysis based on the Michaelis–Menten equation may include the effect of mass transfer resistance through the outer membrane of the enzyme, but the effect is estimated to be small [9]. Detailed mechanistic studies of electron transfer between the electrode and the enzyme can be very complex, especially if the enzymatic reaction is multi-step. In our work, the LDH I substrate reaction proceeds according to a simple mechanism and with high efficiency.

The enzyme LDH catalyzes the reversible conversion between pyruvate and lactate, using the coenzymes NADH/NAD^+:

Pyruvate + NADH → lactate + NAD^+ where:

Pyruvate: main product of glycolysis, substrate of LDH under anaerobic conditions
NADH: reducing equivalent, brings electrons to convert pyruvate to lactate.
Lactate: product of the reaction, important for the regeneration of NAD^+, which allows glycolysis to continue.

This reaction is crucial in anaerobic metabolism in muscles during intense exercise, as it ensures the regeneration of NAD^+ and thus maintains ATP production.

Figure 1 shows cyclic voltammograms of a GC electrode without and with immobilized LDH in phosphate buffer, pH 7, at 50 mV/s. Polymers and other materials are used to immobilize LDH on a GC electrode, as well as other enzymes, and their efficiency depends on the thermodynamics of the redox reaction in the biosensor, the kinetics of electron transfer between the biosensor and the electrode, and the charge transfer within the film on the electrode (biosensor) [10]. Films thicker than a monolayer of electroactive enzyme can often provide a higher enzyme loading per unit electrode area, resulting in higher current peaks.

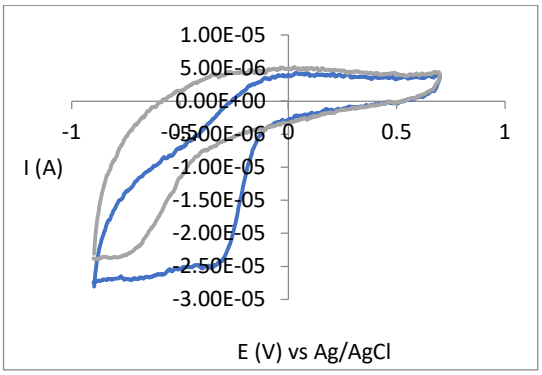

Figure 1. Cyclic voltammogram without enzyme immobilization (gray color) and with immobilized enzyme (blue color)

The catalytic reduction current was monitored by the chronoamperometric method in the presence of different substrate concentrations (1 – 5 mM) in physiological solution. The type of inhibition and the values of the maximum current (I_{max}) and Michaelis-Menten constant (K_m) were determined on the Lineweaver-Burke diagram without and in the presence of the inhibitor, Figure 2.

The Lineweaver-Burk diagram shown in Figure 2 shows that non-competitive inhibition is present in the performed enzyme reactions. In Figure 2, we see that

adding nifuroxazide to the reaction mixture results in the binding of nifuroxazide to the enzyme-substrate complex.

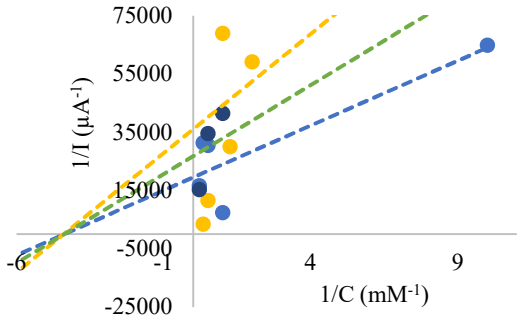

Figure 2. Lineweaver – Burk diagram for determining I_{max} and K_m in the absence and presence of different concentrations of niforoxazide – 0 mM; - 1.025 mM; - 2.023 mM

This type of inhibition is characteristic in that it depends on the presence of the substrate and does not affect the enzyme's affinity for the substrate. In the absence of an inhibitor, the enzyme binds the substrate to form an enzyme-substrate complex, which then catalyzes the reaction and converts the substrate into the product, reflecting the maximum rate at which the enzyme can convert the substrate under optimal conditions. In non-competitive inhibition, the inhibitor specifically binds to the enzyme-substrate complex, changing its conformation. As a result, the enzyme can no longer catalyze the reaction at the same rate as in the absence of inhibition. This reduces Vmax because it reduces the number of functional enzyme sites for catalyzing the reaction. The Michaelis-Menten constant (K_m), which reflects the affinity of the enzyme to the substrate, remains unchanged in noncompetitive inhibition because the enzyme can still bind the substrate with the same affinity, although it cannot catalyze the reaction at the same rate as in the absence of inhibition. A preincubation time of 10 minutes is sufficient to cause a conformational change in the structure of the enzyme and to achieve the binding of nifuroxazide to the ES complex to reduce changes in heart, muscle, or brain cells. Mechanism:

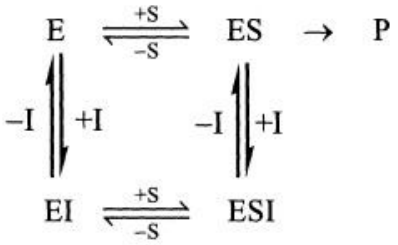

The obtained values of kinetic constants I_{max} and K_m change with the addition of different concentrations of inhibitors, and are shown in Table 1.

Table 1. K_m and I_{max} values in the absence and presence of different concentrations of nifuroxazide

[Nifuroxazide] (mM)	$I_{(max)}$ x10^{-4} (A^{-1})	K_m (mM)
0	5.132	0.22
1.025	3.738	0.22
2.023	2.777	0.22

Nifuroxazide binds to an allosteric site on LDH, altering its catalytic efficiency but not affecting the enzyme's affinity for the substrate. This may have important implications in a metabolic context, as LDH plays a key role in anaerobic glycolysis (the conversion of pyruvate to lactate). Inhibition of LDH could reduce the proliferation of cells that depend on lactate metabolism, which is particularly relevant in investigating the antitumor effects of nifuroxazide. Nifuroxazide is known to be a STAT3 inhibitor, leading to changes in glucose and lipid metabolism in hepatocytes and tumor models [11]. These effects indirectly indicate that the drug may affect glycolytic and fermentative enzymes, including LDH, as LDH is crucial for maintaining anaerobic metabolism in tumor cells. Studies in breast cancer models have shown that nifuroxazide reduces angiogenesis via VEGF signalling [12,13]. The combination of antiangiogenic effects and potential LDH inhibition suggests that the drug may limit the proliferation of lactate-dependent tumor cells. Recent

studies have revealed that NFX has many promising biological activities beyond its classical uses, such as its involvement in anti-inflammatory, antioxidant, and potential roles in inhibiting thyroid, breast, lung, bladder, colon, and liver cancers, as well as osteosarcoma, melanoma, and multiple myeloma. Furthermore, it has promising effects against sepsis-induced organ damage, liver disorders, kidney disease, ulcerative colitis, and immunological disorders. NFX exerts many biological effects, mainly mediated by STAT3 inhibition [14]. Table 2 provides the relationships between the electrochemical effect, biological consequences, and pharmacological implications [15,16].

Table 2. Relationship of the electrochemical effect of nifuroxazide on LDH with biological consequences and pharmacological implications

Electrochemical effect	Biological consequence	Pharmacological implication
Decrease in (I_{max}) (electron transfer capacity)	Reduced NADH oxidation → weaker NAD^+ regeneration	Limits glycolysis in bacteria and tumor cells
Unchanged (Km) (substrate affinity)	Substrate still binds, but enzymatic efficiency decreases	Does not alter binding, only reduces functional enzyme capacity
Non-competitive inhibition of LDH	Disruption of cellular redox balance	Antibacterial effect in intestines; potential antitumor activity
Reduced NAD^+ regeneration	Cells lose the ability to sustain anaerobic metabolism	Tumor cells lose proliferative advantage (Warburg effect)
Blockade of part of the active sites	Fewer available channels for electron transfer	Selective reduction of metabolic activity in pathogenic microorganisms

Electrochemical data clearly show that nifuroxazide acts as a non-competitive inhibitor of LDH. Biologically, this means disruption of NAD^+ regeneration and glycolysis, while pharmacologically, it explains its antibacterial application and potential antitumor perspective. [17,18,19,20].

4. CONCLUSION

Electrochemical data clearly show that nifuroxazide acts as a non-competitive inhibitor of LDH, reducing the electron transport capacity without changing the substrate affinity. Biologically, this means a disruption in the regeneration of NAD^+, which directly affects the metabolism of glycolysis and may have antimicrobial and antitumor significance. This process leads to a permanent blockade of key metabolic reactions, disruption of the redox balance, and death of the bacterial cell.

Acknowledgments

This research was supported by funding through grant number 05-35-3573-1/25 provided by the Federal Ministry of Education and Science, Sarajevo.

Conflicts of Interest

The authors declare no conflict of interest.

5. REFERENCES

[1] L. Di Magno, A. Coluccia, M. Buffanom, S. Ripa, G. La Regina, M. Nalli, F. Di Pastena, G. Canettieri, R. Silvestri, L. Frati, Discovery of novel human lactate dehydrogenase inhibitors: Structure-based virtual screening studies and biological assessment, *Eur J Med Chem.*, 240 (2022), 114605

[2] R. A. Copeland, *Evaluation of Enzyme Inhibitors in Drug Discovery*, Hoboken: John Wiley & Sons, Inc., 2005.

[3] J. R. Seckl, 11beta-hydroxysteroid dehydrogenases: changing glucocorticoid action, *Curr Opin Pharmacol.*, 4 (2004), 6, pp. 597–602

[4] J. Ostojić, S. Herenda, Z. Bešić, M. Miloš, B. Galić, Advantages of an electrochemical method compared to the spectrophotometric kinetic study of peroxidase inhibition by boroxine derivative, *Molecules*, 22 (2017) 7, 1120

[5] S. Herenda, J. Ostojić, E. Hasković, D. Hasković, M. Miloš, B. Galić, Electrochemical investigation of the influence of $K_2[B_3O_3F_4OH]$ on the activity of immobilized superoxide dismutase, *Int J Electrochem Sci.*, 13 (2018) 4, pp. 3279–3287

[6] O. O. Adeyoju, *Development of horseradish peroxidase and tyrosinase-based organic-phase biosensors*, [Doctoral dissertation], Dublin City University, School of Chemical Sciences, Dublin, 1995

[7] S. F. D'Souza, Microbial biosensors, *Biosens Bioelectron.*, 16 (2001) 6, pp. 337–353

[8] G. S. Wilson, editor, *Volume 9: Bioelectrochemistry in: Encyclopedia of Electrochemistry*, Weinheim: Wiley-VCH Verlag GmbH, 2002

[9] T. Ikeda, T. Kurosaki, K. Takayama, K. Kano, K. Miki, Measurement of oxidoreductase-like activity of intact bacterial cells by amperometric method using membrane-coated electrode, *Anal Chem.*, 68 (1996) 1, pp. 192–198.

[10] A. J. Bard, L. R. Faulkner, Electrochemical Methods: Fundamental and Application, 2nd ed., New York: John Wiley & Sons Inc., 2001

[11] Y. Zhu, T. Ye, X. Yu, Q. Lei, F. Yang, Y. Xia, X. Song, L. Liu, H. Deng, T. Gao, C. Peng, W. Zuo, Y. Xiong, L. Zhang, N. Wang, L. Zhao, Y. Xie, L. Yu, Y. Wei, Nifuroxazide exerts potent anti-tumor and anti-metastasis activity in melanoma, *Sci Rep.*, 6 (2016), 20253

[12] D. Mishra, D. Banerjee, Lactate Dehydrogenases as Metabolic Links between Tumor and Stroma in the Tumor Microenvironment, *Cancers*, [Online], 11 (2019) 6, 750

[13] Y. Hou, Y. Zhao, Q. He, M. Wang, Q. Zhang, LDH isozymes as targets for cancer therapy, *J Enzyme Inhib Med Chem.*, [Online], 41 (2026) 1, 2639168

[14] H. S. Althagafy, M. K. A. El-Aziz, I. M. Ibrahim, E. K. Abd-Alhameed, E. H. M. Hassanein, Pharmacological updates of nifuroxazide: Promising preclinical effects and the underlying molecular mechanisms, *Eur J Pharmacol.*, 951 (2023), 175776

[15] J. A. Squella, M. E. Letelier, L. Lindermeyer, L. J. Nuñez-Vergara, Redox behaviour of nifuroxazide: generation of the one-electron reduction product, *Chem Biol Interact.*, 99 (1996) 1–3, pp. 227 - 238

[16] T. H. Ye, F. F. Yang, Y. X. Zhu, Y. L. Li, Q. Lei, X. J. Song, Y. Xia, Y. Xiong, L. D. Zhang, N. Y. Wang, L. F. Zhao, H. F. Gou, Y. M. Xie, S. Y. Yang, L. T. Yu, L. Yang, Y. Q. Wei, Inhibition of Stat3 signaling pathway by nifuroxazide improves antitumor immunity and impairs colorectal carcinoma metastasis, *Cell Death Dis.*, 8 (2017), 1, e2534

[17] J. H. Kang, Y. S. Jang, H. J. Lee, C. Y. Lee, D. Y. Shin, S. H. Oh, Inhibition of STAT3 signaling induces apoptosis and suppresses growth of lung cancer: good and bad, *Lab Anim Res.*, 35 (2019) 30

[18] E. H. M. Hassanein, M. A. Abdel-Reheim, H. S. Althagafy et al., Nifuroxazide attenuates indomethacin-induced renal injury by upregulating Nrf2/HO-1 and cytoglobin and suppressing NADPH-oxidase, NF-κB, and JAK-1/STAT3 signals, *Naunyn Schmiedebergs Arch Pharmaco*l., 397 (2024) 6, pp. 3985–3994

[19] O. Warburg, On the origin of cancer cells, *Science*, 123 (1956), 3191, pp. 309–314.

[20] M. G. Vander Heiden, L. C. Cantley, C. B. Thompson, Understanding the Warburg effect: the metabolic requirements of cell proliferation, *Science*, 324 (2009), 5930, pp. 1029–1033

JST&M 10(2026), 36 – 47

DOI: 10.57131/jstm.2026.10.5

Original scientific paper

OPTIMIZATION OF PROCESS VARIABLES FOR THE PRODUCTION OF FATTY ACID METHYL ESTERS FROM *BIGPOD SESBANIA* SEED OIL

Bukar Wakil[1], Bello Usman Usman Bagudo[2], Abdullahi Muhammad Sokoto[2], Halima Usman[2] Ibrahim Kabir Muduru[3], Nasiru Abdullahi Sani[4]

[1]Federal University Gashua, [2]Usmanu Danfodiyo University, Sokoto, [3]University of Maiduguri, [4]Nigeria Police Academy Wudil Kano, Nigeria

ABSTRACT

This study explores the potential of *Bigpod Sesbania* seed oil as a feedstock for the production of biodiesel. The extracted oil was converted into biodiesel through a transesterification reaction using potassium hydroxide as a catalyst. Or: Response Surface Methodology (RSM) based on the Box–Behnken design was employed to optimize the effects of methanol-to-oil molar ratio, catalyst concentration, reaction time, and reaction temperature on biodiesel yield. The maximum biodiesel yield of 96% was obtained at an 8:1 methanol-to-oil ratio, 0.5 wt.% catalyst, 60 min reaction time, and a temperature of 55 °C. The physicochemical properties of the biodiesel conformed to ASTM D6751 and EN 14214 standards: specific gravity 0.8491, viscosity 4.39 cP, acid value 0.32 mg KOH/g, ash content 0.01%, flash point 166°C, and pour point 4.2 °C. These values indicate high purity and stability. FTIR spectra confirmed the successful conversion of triglycerides to fatty acid methyl esters. GC-MS analysis revealed eight major fatty acid methyl esters (FAMEs), with methyl hexadeca-7,10,13-trienoate (29.80%), methyl (9E,12E)-octadeca-9,12-dienoate (15.97%), and carbonic acid octadecyl prop-1-en-2-yl ester (19.30%) as the dominant components. These unsaturated FAMEs accounted for 99.12% of the total composition, indicating a high degree of unsaturation. This characteristic enhances cold-flow properties but may require antioxidant additives for oxidative stability. Overall, *Bigpod Sesbania* seed oil is validated as a promising non-edible feedstock for high-yield, high-quality biodiesel production with favorable physicochemical properties.

Keywords: *Bigpod Sesbania*, biodiesel, transesterification, RSM optimization, fatty acid methyl esters, ASTM standard

Corresponding Author:
Bukar Wakil
Department of Chemistry, Faculty of Sciences,
Federal University Gashua, Yobe State, Nigeria
PMB 1005, Yobe State, Nigeria
Tel.: +234-8035220412; Fax: +234-80408946
E-mail address: bukar.wakil@fugashua.edu.ng

1. INTRODUCTION

1.1 Background to the Study

Volatile petroleum prices and environmental challenges associated with greenhouse gas (GHG) emissions have driven research into renewable energy [1]. However, the use of edible oils for biodiesel has raised food-versus-fuel debates [2,3]. Hence, non-edible feedstocks are being prioritized. The optimization of biodiesel production from renewable feedstocks has, therefore, become a crucial area of research in addressing the dual challenges of energy insecurity and environmental degradation. Biodiesel, a renewable, biodegradable, and non-toxic fuel

derived from vegetable oils and animal fats, represents a viable alternative to petroleum diesel due to its similar fuel properties and reduced emission profile [4,5]. Biodiesel consists mainly of fatty acid alkyl esters (FAAE), typically produced through transesterification, where triglycerides react with a short-chain alcohol in the presence of a catalyst [6,7]. The reaction yields fatty acid methyl esters (FAME) as the primary product and glycerol as a valuable by-product. Among various methods for converting triglycerides into biodiesel, such as pyrolysis, microemulsion, and catalytic hydrogenation, transesterification remains the most efficient due to its simplicity and high yield [8,9]. The process efficiency is strongly influenced by parameters such as alcohol-to-oil molar ratio, reaction time, temperature, and catalyst concentration [10]. Alkaline catalysts such as potassium hydroxide (KOH) are widely employed due to their high catalytic activity and economic viability [11]. However, excessive catalyst concentration or high free fatty acid (FFA) content in feedstocks can cause soap formation, reducing biodiesel yield. Therefore, optimizing these reaction parameters is essential to enhance conversion efficiency and product quality.

Given the escalating global energy demand and environmental concerns, there is growing interest in non-edible oil feedstocks for biodiesel production. hence, non-edible sources are being prioritized for sustainable biodiesel production [2,3]. One such promising feedstock is *Bigpod Sesbania* (*Sesbania bispinosa*), a fast-growing, nitrogen-fixing legume native to North America [12]. It is highly adaptable to various soils and climatic conditions [13]. It produces abundant seeds, making it an economically attractive and renewable non-edible oil source for biodiesel [14]. Historically cultivated as a cover crop ([15,16], its seed oil has recently gained attention for fuel applications. Recent interest in this plant has shifted toward its potential as a non-edible oil source for biodiesel production. The oil extracted from its seeds contains a high proportion of unsaturated fatty acids, which can yield methyl esters suitable for use in compression ignition (CI) engines after transesterification. However, limited research exists on optimizing the reaction conditions for biodiesel production from *Bigpod Sesbania* seed oil.

Optimization studies are critical for determining the ideal combination of process parameters to maximize biodiesel yield and quality while minimizing production costs. Statistical modeling approaches such as Response Surface Methodology (RSM) are widely used for such optimization because they efficiently evaluate multiple variables and their interactions [17]. Thus, this research focuses on optimizing the transesterification parameters for biodiesel production from *Bigpod Sesbania* seed oil and evaluating the fuel's physicochemical properties for compliance with ASTM biodiesel standards.

2. MATERIAL AND METHODS

2.1 Sample collection and pre-treatment

Seeds of *Bigpod Sesbania* were collected from farmland in Auno village, Konduga Local Government Area, Borno State, northeastern Nigeria. They were authenticated and identified by a botanist from the Department of Plant Science, Usmanu Danfodiyo University, Sokoto. The seeds were washed thoroughly with clean water to remove surface contaminants. They were then shade-dried at ambient temperature for 7 days to reduce moisture content, thereby facilitating easier cracking and preventing microbial growth during storage (Figure 1). After drying, the seeds were manually cracked using a mortar and pestle to loosen the hulls. The cracked seeds were then gently winnowed to separate the kernels from the hulls. The recovered seed kernels were subjected to a second 7-day shade-drying period to eliminate residual moisture, ensuring efficient milling and oil extraction. The dried kernels were crushed into a fine powder using an electric-powered milling machine. The

resulting powder was further dried on a solar dryer for 24 hours to remove any remaining moisture, as excess water can interfere with solvent-based oil extraction.

2.2 Extraction of Oil from *Sesbania bispinosa* Seeds

The powdered seeds of *Sesbania bispinosa* were subjected to the Soxhlet extraction method for oil extraction. Oil was extracted using a conventional Soxhlet apparatus with n-Hexane as the solvent [18].

Figure 1. Seed of Bigpod sesbania

2.3 Characterization of Oil

The physicochemical parameters of the seed oil were determined using the Association of Official Analytical Chemists (AOAC) technique (the acid value by AOAC Ca5a-40, the saponification value by AOAC 920:160, the iodine value by AOAC 920:158, and the peroxide value by AOAC 965.33) [19]. The viscosity and specific gravity were measured using an Ostwald viscometer thermostated at 40°C and a thermal-hydrometer apparatus in accordance with ASTM standards D445 and D1298, respectively, while the density was measured using a density bottle, and the moisture content was determined using the oven method. The ash content was estimated by heating to dryness in a Veisfar muffle furnace.

2.4 Optimization of Transesterification Parameters

The transesterification of *Sesbania bispinosa* seed oil was conducted using methanol and potassium hydroxide (KOH) as a homogeneous catalyst to produce fatty acid methyl esters (biodiesel). The reaction was carried out in a 500 cm^3 round-bottom flask fitted with a reflux condenser to prevent methanol vapor loss during heating [20]. The reaction mixture was stirred using a magnetic stirrer to ensure proper mixing and maintained in a water bath under controlled conditions. Upon completion, the mixture was transferred into a separating funnel and allowed to settle under gravity overnight to facilitate phase separation.

The upper methyl ester layer was carefully collected and heated to remove residual methanol. The biodiesel was then neutralized with dilute phosphoric acid (pH 4.0) and subsequently washed with hot distilled water (1:5 v/v) until the wash water attained a neutral pH of 7.0. The purified methyl esters were dried at 100°C over anhydrous sodium sulfate to eliminate residual moisture. The percentage yield of biodiesel was determined using Equation (1):

$$\text{Biodiesel yield (\%)} = \frac{\text{Weight of biodiesel}}{\text{Weight of oil}} \times 100 \qquad (1)$$

[20]

Optimization of the transesterification parameters was performed using the Box–Behnken Design (BBD) under Response Surface Methodology (RSM) to assess the individual and interactive effects of the process variables on biodiesel yield. The Box–Behnken Design, a rotatable second-order statistical model, provides an efficient means of evaluating quadratic effects with a minimal number of experimental runs, while the Response Surface Methodology offers a mathematical and statistical framework for analyzing and optimizing chemical processes [21]. Four independent process variables' reaction time (30–90 min), catalyst concentration (0.1–0.5 wt%), methanol-to-oil molar ratio (4:1–8:1), and reaction temperature (45–65°C) were selected based on preliminary studies. Each variable was examined at three coded levels (low, medium, and high) to

determine its influence on biodiesel production. The operating parameters selected for the Box-Behnken Design, together with their investigated ranges, are presented in Table 1. The experimental design matrix generated by the BBD was employed to conduct the transesterification runs, and the corresponding biodiesel yields were used as response data for RSM-based model development. This approach enabled the identification of optimal process conditions necessary to achieve high conversion efficiency and superior biodiesel quality.

Table 1. Effect of operating parameters on yield

Factors	Low level	High level
Time (mins)	30	90
catalyst (wt%)	0.1	0.5
MeOH:Oil	4:1	8:1
Temp (°C)	45	65

2.5 Determination of Biodiesel Properties

The physicochemical properties of the biodiesel were determined according to ASTM standard methods and AOAC (2000) official procedures. The kinematic viscosity was determined by the ASTM D-445 method, the density was determined by the ASTM D-1298 method, and the pour point determination was made using the ASTM D-97 method. The flash point of the fuel was determined by ASTM D-93, the value of cloud point was estimated according to ASTMD-2500 and the acid value was measured following the ASTM D-664 method. The specific gravity was ascertained using AOAC 920.212 and iodine value using AOAC 920:159. The moisture content was determined using the air-oven method using the Rotary Evaporator Oven (BTOV 1423), while the cetane number (CN) was calculated by the equation developed by [22].

2.6 FT–IR Spectroscopy

Fourier Transform Infrared (FTIR) spectroscopy was used to identify the functional groups present in the produced biodiesel. Characteristic absorption bands corresponding to specific molecular vibrations (e.g., C=O stretching, C–H bending) were analyzed to confirm the conversion of triglycerides to fatty acid methyl esters (FAMEs).

2.6.1 Fourier Transform Infrared (FTIR) Spectroscopic Analysis

FTIR spectra were recorded on an Agilent Cary 630 FTIR spectrometer controlled with Microlab software. Samples were measured using the ATR accessory with a diamond crystal. Spectra were collected over the range 4000–400 cm^{-1} at 4 cm^{-1} resolution with 32 co-added scans; backgrounds were recorded immediately before sample measurements. Each sample was measured in triplicate by removing and reapplying the sample to the ATR crystal to assess reproducibility. Spectra were converted to absorbance, baseline corrected (polynomial order 2), and lightly smoothed (Savitzky–Golay, window 7, 2nd order) in Microlab. Peak positions are reported as the mean of three replicates ± standard deviation and assigned by comparison to literature values.

2.6.2 Gas Chromatography - Mass Spectrometry

GC-MS analysis was conducted on an Agilent 7890A GC-5977 MSD system with an HP-5ms column (30 m × 0.25 mm × 0.25 µm). Helium carrier gas flowed at 1.16 mL/min. The injector (split less mode) and transfer line were set at 280°C. The oven program was: 50 °C (2 min) to 280°C at 10°C/min (5 min hold). The MSD operated at 70 eV (EI) with the ion source at 230°C and quadrupole at 150°C. Mass spectra were acquired over m/z 50–650. Compound identification used the NIST library.

2.7 Gas Chromatography-Mass Spectrometry (GC-MS) Analysis

GC-MS analysis was conducted on an Agilent 7890A GC-5977 MSD system equipped with an HP-5ms column (30 m × 0.25 mm × 0.25 µm). Helium was used as the carrier gas at a flow rate of 1.16 mL/min. The injector operating in splitless mode and the transfer line were both set at 280°C. The oven temperature program was as follows: initial temperature of 50°C held for 2 min, then ramped to 280°C at 10°C/min, with a final hold of 5 min. The mass selective detector (MSD) operated in electron ionization (EI) mode at 70 eV, with the ion source at 230°C and the quadrupole at 150°C. Mass spectra were acquired over a range of m/z 50–650. Compound identification was performed using the NIST mass spectral library.

3. Results and Discussion

3.1 Physical and chemical characteristics of seed oils and biodiesel

The seed oils were evaluated by measuring their physicochemical characteristics and functional groups using FT-IR analysis. The biodiesel derived from seed oils was further studied for physicochemical characteristics, functional groups, and fatty acid composition. The physicochemical properties of Bigpod sesbania seed oil, determined in this study, are presented in Table 2

The oil content is an important consideration when selecting plant seeds as a potential feedstock for biodiesel and other industrial applications. A 20% oil yield was recovered by Soxhlet extraction of Bigpod sesbania seeds, which is much higher than the 12% oil yield reported by [23]. But within the 15-20% range reported by other researchers [24]. The oil content is substantial and similar to that of cottonseed oil, as reported by [25].

Table 2. Physicochemical properties of *Bigpod sesbania* seed oil.

Parameters	Values
Specific Gravity	0.91 ± 0.01
Density (g/cm^3)	0.89 ± 0.01
Viscosity @ 40 C (mPa.s)	30.5 ± 0.40
Acid Value (mg KOH/g)	2.4 ± 0.05
Free fatty acid	1.2 ± 0.03
Ash content	0.17 ± 0.01
Moisture	0.07 ± 0.005
Saponification Value (mg KOH/g)	189 ± 1.50
Flash point (°C)	205 ± 2.0
Pour point (°C)	-6 ± 0.5
Ester value (mg KOH/g)	186.6 ± 1.0
Average Iodine Value (IV)	32.2 g I_2/100g

The density (0.89 g/cm³) falls within the typical vegetable oil range (0.882–0.925 g/cm³) and agrees with *Jatropha curcas* (0.87–0.91 g/cm³) and soybean (0.88–0.90 g/cm³) oils [26].

The acid value (2.4 mg KOH/g; FFA 1.2%) is below the 2% threshold requiring pretreatment, making the oil suitable for direct base-catalyzed transesterification [27,28]. The saponification value (189 mg KOH/g) aligns with jatropha (193.55 mg KOH/g) and castor (202 mg KOH/g) oils [29]. The iodine value (32.2 g I_2/100g) indicates moderate unsaturation, balancing oxidative stability and cold-flow performance [30]. The flash point (205°C) confirms thermal stability and safe handling [26]. Moisture content (0.07%) was low compared to other seed oils [31]. promoting high biodiesel yield.

3.2 Optimal biodiesel production parameters of *Bigpod sesbania* seed oil

The experimental design matrix and the corresponding biodiesel yields obtained under the investigated transesterification conditions are presented in Table 3, while the analysis of variance (ANOVA) and response surface regression results for the developed model are presented in Table 4. Transesterification optimization identified the maximum biodiesel yield of 96% at 60 min, 0.5 wt% KOH, 8:1 methanol-to-oil ratio, and 55°C (Table 4, Run 4). Temperature significantly influenced yield, with 55°C promoting faster glycerol separation [32]. Excessive catalyst (0.5 wt% at 30 min) gave a lower yield (71%) due to soap formation, while a higher acid value promoted saponification, drastically reducing ester yield.

Table 3. Process evaluation parameters and experimental results

Run Order	Time (mins)	Catalyst Conc (wt%)	MeOH:Oil	Temp. (^{0}C)	Methyl ester yield (wt %)
					Experimental
1	30	0.1	6:1	55	86
2	90	0.1	6:1	55	87
3	30	0.5	6:1	55	71
4	90	0.5	6:1	55	94
5	60	0.3	4:1	45	71
6	60	0.3	8:1	45	76
7	60	0.3	4:1	65	71.4
8	60	0.3	8:1	65	72
9	30	0.3	6:1	45	76
10	90	0.3	6:1	45	78.5
11	30	0.3	6:1	65	69.5
12	90	0.3	6:1	65	72
13	60	0.1	4:1	55	76.3
14	60	0.5	4:1	55	80
15	60	0.1	8:1	55	78
16	60	0.5	8:1	55	96
17	30	0.3	4:1	55	59
18	90	0.3	4:1	55	83
19	30	0.3	8:1	55	41
20	90	0.3	8:1	55	78
21	60	0.1	6:1	45	94
22	60	0.5	6:1	45	94
23	60	0.1	6:1	65	85
24	60	0.5	6:1	65	76
25	60	0.3	6:1	55	67
26	60	0.3	6:1	55	67
27	60	0.3	6:1	55	66.6

3.4 Response Surface Regression Analysis

The ANOVA results (Table 5) showed the regression model was highly significant ($p < 0.05$) with $R^2 = 98.93\%$, confirming a strong correlation between experimental and predicted values. Reaction time and temperature significantly affected yield ($p < 0.001$), while catalyst and methanol-to-oil ratio were not significant at the linear level. Quadratic effects of catalyst and temperature were highly significant, indicating excessive levels of lower yield due to soap formation [33].

The characteristic FTIR absorption bands identified for the produced biodiesel are presented in Table 6.

Table 4. Response Surface Regression: yield versus Time, Catalyst, Methanol, Temperature

Source	DF	Adj SS	Adj MS	F-Value	P-Value	SIGNIFICANT
Model	14	2631.58	187.97	79.04	0.000	S
Linear	4	880.38	220.09	92.55	0.000	S
Time	1	665.71	665.71	279.92	0.000	S
Catalyst	1	1.07	1.07	0.45	0.514	Ns
Methanol	1	2.28	2.28	0.96	0.347	Ns
Temp	1	211.32	211.32	88.85	0.000	S
Square	4	1500.57	375.14	157.74	0.000	S
Time*Time	1	7.78	7.78	3.27	0.096	Ns
Catalyst*Catalyst	1	1202.32	1202.32	505.55	0.000	S
Methanol*Methanol	1	6.51	6.51	2.74	0.124	Ns
Temp*Temp	1	162.05	162.05	68.14	0.000	S
2-Way Interaction	6	250.64	41.77	17.56	0.000	S
Time*Catalyst	1	123.63	123.63	51.98	0.000	S
Time*Methanol	1	42.26	42.26	17.77	0.001	S
Time*Temp	1	0.05	0.05	0.02	0.884	Ns
Catalyst*Methanol	1	21.30	21.30	8.96	0.011	S
Catalyst*Temp	1	58.55	58.55	24.62	0.000	S
Methanol*Temp	1	4.85	4.85	2.04	0.179	Ns
Error	12	28.54	2.38			
Lack-of-Fit	10	28.53	2.85	481.39	0.002	S
Pure Error	2	0.01	0.01			
Total	26	2660.12				

Model Summary S= 1.54215 R^2 = 98. 93% R^2(adj) 97.68% R^2(pred) 93.82%

Table 5. Summary of Significant Model Terms for Biodiesel Yield

Source	DF	Adj SS	Aji MS	F-Value	P-Value
Model	9	2606. 77	289.64	92.28	0.000
Linear	2	877. 02	438.51	139.72	0.000
Time	1	665.71	665.71	212.10	0.000
Temp	1	211.32	211.32	67.33	0.000
Square	2	1479.16	739.58	235.64	0.000
Catalyst*Catalyst	1	1437.86	1437.86	458.13	0.000
Temp*Temp	1	192.66	192.66	61.38	0.000
2-Way Interaction	5	250.58	50.12	15.97	0.000
Time*Catalyst	1	123.63	123.63	39.39	0.000
Time*Methanol	1	42.26	42.26	13.46	0.002
Catalyst*Methanol	1	21.30	21.30	6.79	0.018
Catalyst*Temp	1	58.55	58.55	18.66	0.000
Methanol*Temp	1	4.85	4.85	1.55	0.231
Error	17	53.36	3.14		
Lack-of-Fit	15	53.34	3.56	600.12	0.002
Pure Error	2	0.01	0.01		
Total	26	2660.12			

Model Summary S= 1.77160 R^2 = 97.99% R^2(adj) 96.93% R^2(pred) 94.39%

Table 6. FTIR Analysis of Biodiesel Derived from *Sesbania* Oil

Functional Group	Type of Vibration	Wavenumber (cm^{-1})
C–H	Stretching	3100
C–H	Asymmetric stretching	2926
C-H	Stretching	2851
C=O	Streching	1748
CH_2	Bending	1459

3.6.1 The regression equation after removing insignificant terms

Yield (%) = 66.979 + 7.448 × Time − 4.196 × Temp + 14.989 × (Catalyst)² + 5.487 × (Temp)² + 5.559 × (Time × Catalyst) + 3.250 × (Time × Methanol) + 2.308 × (Catalyst × Methanol) − 3.826 × (Catalyst × Temp) − 1.101 × (Methanol × Temp)

3.6.2 Significance of the Model

The model was highly significant ($p < 0.05$) with F-value of 92.28, confirming the quadratic model is superior to the mean response (Meher et al., 2006). R^2 = 97.99% indicates the model explains nearly 98% of yield variation. Close agreement between adjusted R^2 (96.93%) and predicted R^2 (94.39%) confirms predictive accuracy without overfitting [6].

3.6.3 Linear Effects

Both reaction time ($F = 212.10$, $p < 0.001$) and temperature ($F = 67.33$, $p < 0.001$) had a statistically significant influence on biodiesel yield. Among the linear terms, reaction time exhibited the largest F-value, indicating the strongest relative effect on yield within the studied range. This is likely because longer reaction durations improve contact between reactants, enhancing conversion efficiency. Temperature also positively influenced yield by improving reaction kinetics; however, excessive temperatures may lead to methanol vaporization, reducing the effective alcohol-to-oil ratio and thus lowering yield [36].

3.6.4 Quadratic (Square) Effects

The significant quadratic term for catalyst concentration ($F = 458.13$, $p < 0.001$) indicates a curvilinear relationship, with yield increasing up to an optimum (approximately 0.3–0.5 wt%) and declining beyond due to soap formation. Similarly, the quadratic term for temperature ($F = 61.38$, $p < 0.001$) confirms a parabolic response, predicting an optimum around 55°C, where kinetics are favorable, and methanol loss is minimized [37].

3.6.5 Two-Way Interaction Effects

Time×Catalyst ($F = 39.39$, $p < 0.001$) was the strongest interaction—catalyst effectiveness depends on reaction duration. Time×Methanol ($F = 13.46$, $p = 0.002$), Catalyst×Methanol ($F = 6.79$, $p = 0.018$), and Catalyst×Temp ($F = 18.66$, $p < 0.001$) were also significant. Methanol×Temp was insignificant ($p = 0.231$) [6].

3.6.6 Lack-of-Fit and Model Adequacy

The lack-of-fit test was significant ($p = 0.002$), suggesting that the model may not fully capture all sources of variation. However, the pure error was very small (0.01), and the low standard deviation ($S = 1.7716$) indicates acceptable model precision for predictive purposes [37].

3.7 Contour Plots for Significant Interaction Effects

Contour plots (Fig. 2-5) revealed significant interaction effects among variables. Yield increased with time up to 90 min and catalyst up to 0.3 wt%, beyond which soap formation reduced yield [38]. Methanol-to-oil ratio up to 6:1 improved yield, while excess methanol complicated glycerol separation [39]. Temperature up to 55°C enhanced yield, but higher temperatures promoted methanol evaporation [6]. Optimal conditions were: 0.3 wt% catalyst, 6:1 methanol-to-oil ratio, 90 min, and 55°C (R^2 = 97.99%). FTIR confirmed

successful transesterification: the carbonyl peak shifted from 1742 cm^{-1} (oil) to 1748 cm^{-1} (biodiesel), indicating conversion to methyl esters, while disappearance of the O–H band confirmed FFA removal [40,41].

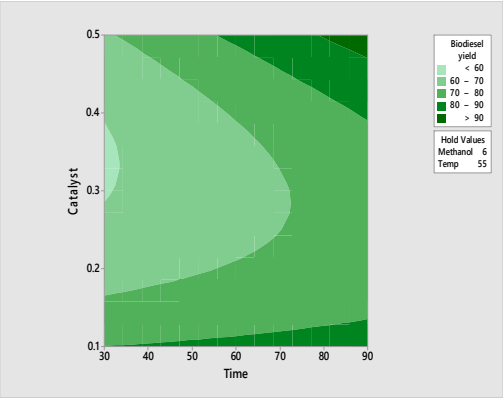

Figure 2. Catalyst and Time

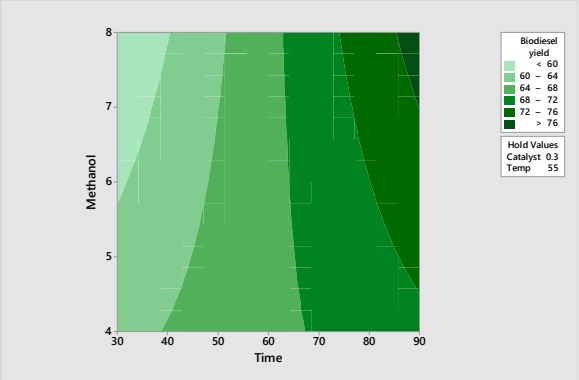

Figure 3. Oil Ratio and Time

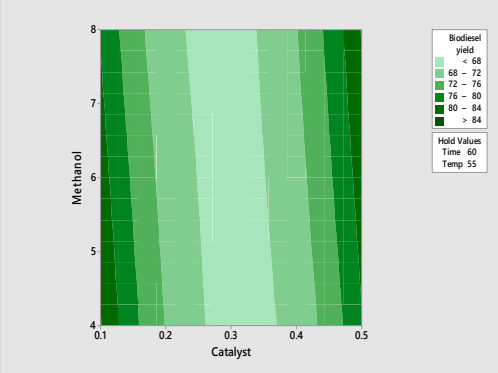

Figure 4. Oil Ratio and Catalyst

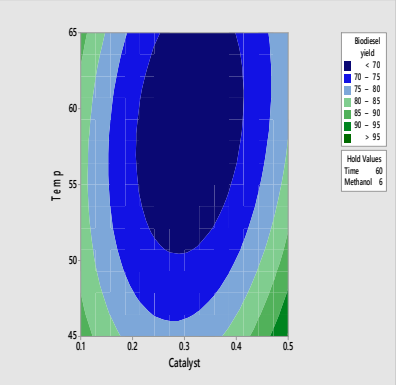

Figure 5. Temp. and Catalyst

FTIR analysis confirmed successful transesterification. The oil spectrum showed a carbonyl (C=O) stretch at 1742 cm^{-1} and C–H stretches at 2922 and 2851 cm^{-1}, characteristic of triglycerides. After transesterification, the biodiesel spectrum exhibited a shift of the carbonyl peak to 1748 cm^{-1}, confirming conversion to methyl esters [40,41]. The =C–H stretch shifted to 3100 cm^{-1}, indicating retained unsaturation. The disappearance of the O–H band (~3400 cm^{-1}) confirmed effective removal of free fatty acids and moisture. These results confirm efficient conversion of *Bigpod Sesbania* seed oil to high-purity biodiesel.

3.8 GC–MS Analysis and Discussion

The GC–MS chromatogram of the trans esterified *Bigpod Sesbania* seed oil revealed a mixture of fatty acid methyl esters (FAMEs) and oxygenated long-chain esters, confirming successful transesterification of the triglycerides into biodiesel. The identified fatty acid methyl esters (FAMEs) and their relative abundances determined by GC–MS analysis are presented in Table 7. Eight major components were identified, with molecular chain lengths ranging from C_{17} to C_{23}. The most abundant compounds were methyl hexadeca-7,10,13-trienoate (29.80%), methyl (9E,12E)-octadeca-9,12-

dienoate (15.97%), and carbonic acid, octadecyl prop-1-en-2-yl ester (19.30%).

The dominance of methyl hexadecatrienoate and methyl linoleate indicates that the biodiesel possesses a high level of unsaturation, characterized by multiple double bonds. Such polyunsaturated esters improve cold-flow properties, fuel atomization, and combustion efficiency, but they may reduce oxidative stability due to the susceptibility of double bonds to oxidation during storage [28,40].

The detection of carbonic and oxalic acid esters (approximately 34% of the total composition) suggests the presence of oxygenated derivatives, possibly formed through side reactions involving alcohol intermediates and residual CO_2 during transesterification. These compounds enhance fuel lubricity and combustion performance due to their oxygen-rich structures, though excessive concentrations could slightly increase viscosity.

The absence of triglyceride peaks indicates complete conversion of the oil to methyl esters, demonstrating high reaction efficiency. The overall molecular weight distribution (C_{16}–C_{23}) aligns with values typical of biodiesels derived from long-chain plant oils and agrees with previous studies on *Sesbania* and other non-edible feedstocks [41]. The GC–MS data confirm that *Bigpod Sesbania* seed oil is a promising feedstock for biodiesel production, producing fuel rich in unsaturated methyl esters with favorable ignition quality, low-temperature fluidity, and acceptable viscosity. Nevertheless, the high degree of unsaturation suggests that antioxidant additives or blending with more saturated biodiesel could be recommended to improve oxidative stability during long-term storage. The fuel property profile of *Bigpod Sesbania* biodiesel demonstrates a highly unsaturated composition (99%), dominated by polyunsaturated esters such as methyl hexadeca-7,10,13-trienoate (C16:3) and methyl (9E,12E)-octadeca-9,12-dienoate (C18:2), along with a notable fraction of oxygenated monounsaturated esters. This composition enhances low-temperature operability, promotes complete combustion, and supports efficient atomization, all of which are essential for improved engine performance [28,40].

Table 7. Fatty Acid methyl esters (FAME) profile of Biodiesel from *Bigpod Sesbania* Seed Oil

Compound Name	Molecular formula	Area %
Methyl hexadeca 7,10,13 trienoate	$C_{17}H_{28}O_2$	29.80
Methyl (9E,12E)-octadeca-9,12 dienoate	$C_{19}H_{34}O_2$	15.97
Carbonic acid, octadecyl prop-1-en -2-yl ester	$C_{22}H_{42}O_3$	19.3
Carbonic acid, eicosyl vinyl ester	$C_{23}H_{44}O_3$	15.36
Carbonic acid, octadecyl vinyl ester	$C_{21}H_{40}O_3$	10.02
Oxalic acid, allyl undecyl ester	$C_{21}H_{38}O_3$	1.60
Oxalic acid, isobutyl tridecyl ester	$C_{19}H_{36}O_4$	2.83
Oxalic acid, dodecyl propyl ester	$C_{17}H_{32}O_4$	4.24

4. CONCLUSIONS

This study successfully produced high-quality biodiesel from *Bigpod Sesbania* seed oil via KOH-catalyzed transesterification. Optimal conditions (8:1 methanol-to-oil ratio, 0.5 wt% KOH, 60 min, 55°C) yielded 96% biodiesel. The biodiesel met ASTM D6751 and EN 14214 standards (viscosity 4.39 cP, acid value 0.32 mg KOH/g, flash point 166°C, cetane number 56.4). FTIR confirmed conversion to methyl esters, and GC-MS revealed polyunsaturated FAMEs. *Bigpod Sesbania* is a viable non-edible feedstock for sustainable biodiesel production.

Conflict of Interest

The authors declare no conflict of interest.

5. REFERENCE

[1] M. J. Abedin, H. H. Masjuki, M. A. Kalam, A. Sanjid, S. M. A. Rahman, and I. M. Rizwanul Fattah, Performance, emissions, and heat losses of palm and jatropha biodiesel blends in a diesel engine, *Ind. Crops Prod.*, 59 (2014), pp. 96–104, doi: 10.1016/j.indcrop.2014.05.001

[2] M. M. Azam, A. Waris, and M. N. Nahar, Prospects and potential of fatty acid methyl ester of some non-traditional seed oils for use as a biodiesel in India, *Biomass Bioenergy*, 29 (2005) 4, pp. 293–302, doi: 10.1016/j.biombioe.2005.05.001

[3] R. A. Voloshin, V. D. Kreslavski, S. K. Zharmukhamedov, V. S. Bedbenov, S. Ramakrishna, and S. I. Allakhverdiev, Photoelectrochemical cells based on photosynthetic systems: a review, *Biofuel Res. J.*, 6 (2015), pp. 227–235

[4] A. E. Atabani, A. S. Silitonga, A. B. Irfan, T. M. I. Mahlia, H. H. Masjuki, and S. Mekhilef, A comprehensive review on biodiesel as an alternative energy resource and its characteristics, *Renew. Sustain. Energy Rev.*, 16 (2012) 4, pp. 2070–2093

[5] S. P. Gouda, A. Dhakshinamoorthy, and S. L. Rokhum, Metal–organic framework as a heterogeneous catalyst for biodiesel production: A review, *Chem. Eng. J. Adv.*,12(2022), 100415 doi: 10.1016/j.ceja.2022.100415

[6] F. Ma and M. A. Hanna, Biodiesel production: A review, *Bioresour. Technol.*, 70 (1999) 1, pp. 1–15,

[7] D. Kumar, A. Ali, *Biomass Bioenergy*, 46 (2012), pp. 459–468

[8] A. Demirbas, Progress and recent trends in biodiesel fuels, Energy Convers. Manag., 50 (2009) 1, Pp. 14–34

[9] X. Fan, *Optimization of biodiesel production from crude cotton seed oil and waste vegetable oil; conventional and ultrasonic irradiation methods*, [Ph.D. thesis], Dept. Food Technol., Clemson Univ., 2008.

[10] L. Adhani, S. Nurbayati, C. O. Oktaviana, Pembuatan Biodiesel dengan Cara Adsorpsi dan Transesterifikasi dari Minyak Goreng Bekas (Biodiesel Production by Adsorption and Transesterification from Used Cooking Oil), *J. Tek. Kim.*, 15 (2016), 2, pp. 34–43

[11] Y. Lotero, D. E. Liu, K. Lopez, K. Suwannakarn, D. A. Bruce, and J. G. Goodwin Jr., Synthesis of biodiesel via acid catalysis, *Ind. Eng. Chem. Res.*, 44 (2005) 14, pp. 5353–5363

[12] C. M. Sheahan, *Plant Guide for Bigpod Sesbania (Sesbania exaltata),* Cape May Plant Materials Center, Cape May, NJ, USA, 2013.

[13] C. T. Bryson, Interference and critical time of removal of hemp sesbania (Sesbania exaltata) in cotton (Gossypium hirsutum), *Weed Technol.*, 4 (1990) 4, pp. 833–837

[14] J. A. Duke, Sesbania, in: Handbook of Energy Crops, NewCROP (New Crops Resource Online Program), Purdue Univ. Center for New Crops and Plant Products, 1983

[15] O. N. Allen, E. K. Allen, *The Leguminosae: A Source Book of Characteristics, Uses, and Nodulation*, London, Macmillan, 1981

[16] D. O. Evans, P. P. Rotar, *Sesbania in Agriculture*, Boulder, CO: Westview Press, 1987

[17] G. Vicente, M. Martínez, J. Aracil, Integrated biodiesel production: a comparison of homogeneous catalyst systems, *Bioresour. Technol.*, 92 (2004) 3, pp. 297–305 doi: 10.1016/j.biortech.2003.08.014

[18] A. A. Alsaedi, H. M. Sohrab, V. Balakrishnan, S. M. AbdulHakim, M. Zaini, M. Makhtar, and N. Ismail, Extraction and separation of lipids from municipal sewage sludge for biodiesel production: kinetics and thermodynamics modeling, *Fuel*, 325 (2022), 124946, 2022. doi: 10.1016/j.fuel.2022.124946

[19] AOAC, *Official Methods of Analysis*, 13th ed., Washington, DC: Association of Official Analytical Chemists, 2000

[20] M. A. Sokoto, L. G. Hassan, M. A. Salleh, S. M. Dangoggo, and H. G. Ahmad, Quality assessment and optimization of biodiesel from Lagenaria vulgaris (calabash) seeds oil, *Int. J. Pure Appl. Sci. Technol.*, 15 (2013) 1, pp. 55–66

[21] R. H. Myers, D. C. Montgomery, C. M. Anderson-Cook, *Response Surface Methodology: Process and Product Optimization Using Designed Experiments*, 4th ed., John Wiley & Sons, 2016

[22] V. Patel, Cetane number of New Zealand diesel, Report, Office of Chief Gas Engineer, Energy Inspection Group, Ministry of Commerce Press, Wellington, New Zealand, 1999

[23] F. Anwar, U. Rashid, Ashraf M, et al. Okra (Hibiscus esculentus) seed oil for biodiesel production, *Appl. Energy*, 87 (2010) 3, pp. 779–785, doi: 10.1016/j.apenergy.2009.09.020

[24] R. L. Jarret, M. L. Wang, I. J. Levy, Seed oil and fatty acid content in Okra (Abelmoschus esculentus) and related species, J. Agric. Food Chem., 59 (2011) 8, pp. 4019–4024 doi:10.1021/jf104590u

[25] A. Muhammad, K. Bello, A. D. Tambuwal, Assessment and optimization of conversion of L. siceraria seed oil into biodiesel using CaO on Kaolin as heterogeneous catalyst, *Int. J. Chem. Technol.*, 7 (2015) 1, pp. 1–11 doi:10.3923/ijct.2015.1.11

[26] G. Knothe, Biodiesel and renewable diesel: A comparison, *Prog. Energy Combust. Sci.*, 36 (2010) 3, pp. 364–373

[27] A. S. Ramadhas, S. Jayaraj, and C. Muraleedharan, Biodiesel production from high FFA rubber seed oil, *Fuel Process. Technol.*, 84 (2005) 4, pp. 335–340, doi: 10.1016/j.fuel.2004.09.016

[28] G. Knothe, Dependence of biodiesel fuel properties on the structure of fatty acid alkyl esters, *Fuel Process. Technol.*, 86 (2005) 10, pp. 1059–1070

[29] A. Demirbas, Biodiesel fuels from vegetable oils via catalytic and non-catalytic supercritical alcohol transesterifications and other methods: a survey, *Energy Convers. Manag.*, 44 (2003) 13, pp. 2093–2109 doi:10.1016/S0196-8904(02)00234-0

[30] A. Demirbas, Relationships derived from physical properties of vegetable oil and biodiesel fuels, *Fuel*, 87 (2008) 8-9, pp. 1743–1748, doi: 10.1016/j.fuel.2007.08.007.

[31] A. U. Ofoefule, C. N. Ibeto, U. C. Okoro, and O. D. Onukwuli, Biodiesel production from tigernut (Cyprus esculentus) oil and characterization of its blend with petrodiesel, Phys. Rev. Res. Int., (2013) 2, pp. 145–153

[32] P. K. Gupta, R. Kumar, P. S. Panesar, and V. K. Thapar, Parametric studies in biodiesel prepared from rice bran oil, *Agric. Eng. Int. CIGR J. Sci. Res. Dev.*, 9 (2007), EE 06-007

[33] B. Aminu, M. O. Muhammad, H. G. Lawal, and A. A. Adamu, Optimization of process variables in acid-catalysed in situ transesterification of Hevea brasiliensis (rubber tree) seed oil into biodiesel, *Biofuels,* [Online], *8* (2017) 5, pp. 585-594, doi: 10.1080/17597269.2016.1242689

[34] D. Y. C. Leung, X. Wu, and M. K. H. Leung, A review on biodiesel production using catalyzed transesterification, *Appl. Energy*, 87 (2010) 4, pp. 1083–1095, doi: 10.1016/j.apenergy.2010.10.006

[35] U. Rashid, F. Anwar, G. Knothe, Evaluation of biodiesel obtained from cottonseed oil, *Fuel Process. Technol.*, 90 (2009) 9, pp. 1157–1163 doi:10.1016/j.fuproc.2009.05.016

[36] L. C. Meher, D. Vidya Sagar, and S. N. Naik, Technical aspects of biodiesel production by transesterification—a review, *Renew. Sustain. Energy Rev.*, 10 (2006)3, pp. 248–268, doi:10.1016/j.rser.2004.09.002

[37] D. C. Montgomery, *Design and Analysis of Experiments*, 9th ed., Wiley, 2017

[38] B. Freedman, R. O. Butterfield, E. H. Pryde, Transesterification kinetics of soybean oil, *JAOCS*, 63 (1986) 10, pp. 1375–1380

[39] B. R. Moser, Biodiesel production, properties, and feedstocks, in book: In Vitro Cell. Dev. Biol. – Plant, eds. Dwight Tomes, Prakash Lakshmanan, David Songstad, NY, Springer New York, pp. 285–347, 2009

[40] G. Knothe, Analyzing biodiesel: standards and other methods, J. Am. Oil Chem. Soc., 83 (2006), 10, pp. 823–833

[41] M. J. Ramos, C. M. Fernández, A. Casas, L. Rodríguez, Á. Pérez, Influence of fatty acid composition on biodiesel properties, Bioresour. Technol., 100 (2009) 1, pp. 261–268

JST&M 10(2026), 48 – 55
DOI: 10.57131/jstm.2026.10.6

Professional paper

INFLUENCE OF PROCESS PARAMETERS ON THE PHYSICAL AND MECHANICAL PROPERTIES OF EXTRUDED POLYSTYRENE

Sarah Lenasi

TEMAX BH d.o.o., Bosnia and Herzegovina

ABSTRACT

In this work, I aim to examine the various influences of process parameters on the physical and mechanical properties of extruded polystyrene. Since XPS belongs to the group of thermoplastic polymers, its properties are significantly affected by thermal treatment, particularly temperature and pressure. However, in addition to these key factors, this paper also aims to examine the impact of other parameters. Production, sampling, parameter monitoring, and sample testing were conducted in the production facility and the laboratory for construction materials within the TEMAX BH d.o.o. company. The findings of this research are expected to provide valuable insights into optimizing manufacturing conditions to enhance XPS performance, thereby improving material efficiency and expanding its potential applications in the construction and insulation industries.

Keywords: XPS, process parameters, extruded polystyrene, compressive strength, and melt flow index.

Corresponding Author:
Sarah Lenasi
TEMAX BH d.o.o., Bosnia and Herzegovina
26 ulica br.15, Orašje, Bosnia and Herzegovina
Tel.: 061/053-116
E-mail address: sarahlenasi@hotmail.com

1. INTRODUCTION

XPS, also known as extruded polystyrene, is a thermal insulation material widely used in building construction and beyond.

The production process of XPS rigid foam involves the following steps:

1. Thermoplasticization of solid polymer and additives;
2. Injection of a physical foaming agent and initial mixing;
3. Cooling the resulting mixture to optimal foaming temperatures, ensuring complete dissolution of the foaming agent;
4. Foam stabilization, shaping, and finishing to final dimensions [1].

Solid XPS foam is produced through a continuous extrusion process in which solid polystyrene granules are melted with various additives to enhance the process and production efficiency. The most common additives include foaming agents, lubricants, antioxidants, plasticizers, blowing agents, colorants, and flame retardants, among others. Each additive has a recommended usage and dosage. For example, when selecting a flame retardant, an increase in thermal stability typically results in a decrease in its reactivity or activity [2-4].

Blowing agents, which are gases used to create a cellular structure within the foam, play a key role in determining the material's thermal properties. Using gases with low

thermal conductivity improves thermal insulation performance. "Hydro nuc" (H.N) is a chemical nucleating agent that releases CO_2, ensuring a very fine, dense foam structure with a high nucleation degree [5,6]. The XPS production process begins with the introduction of polystyrene raw material and auxiliary components in a specific ratio via an automated dosing system. The polystyrene granules are fed into the primary extruder under controlled temperature and pressure conditions, where they are heated and melted along with additives into a viscous fluid. This molten mixture is then filtered and transferred to the secondary extruder, where it undergoes further melting and compaction. Using controlled heating and pressure, the molten mass is extruded through a wide-slot nozzle to form the foam. The flow of XPS foam is regulated by the screws of the extruder head. After passing through the calibrator, the foam mixture is considered a semi-finished product and is transported in a continuous strip to a machine for surface treatment and cutting. During transportation, the semi-finished product cools rapidly, which may cause slight variations in thickness and width, though these are generally negligible. The production line can also include additional surface treatments, such as creating a waffle texture or cutting channels into the surface. Finally, the product is cut to the desired board length [7-10]

2. EXPERIMENTAL

The experimental phase begins with the establishment and monitoring of process parameters, which are defined based on several factors. One of the key factors is the polymer granulate itself, particularly its technical characteristics and processing requirements, including its rheological properties, such as the melt flow index (MFI). Once sampling is completed, the XPS panel is taken to the laboratory, where it is measured, weighed, and prepared to the appropriate dimensions. According to BAS EN 826:2014, "Thermal Insulating Products for Building Applications – Determination of Compression Behavior," the test specimens must be precisely cut into square shapes with the specified dimensions:

1. 50 mm × 50 mm or
2. 100 mm × 100 mm or
3. 150 mm × 150 mm or
4. 200 mm × 200 mm or
5. 300 mm × 300 mm [11].

Compressive strength was tested at a deformation of 10%. The compressive stress at 10% strain, σ_{10}, in kPa, is calculated according to Eq. (1):

$$\sigma_{10} = 10^3 \frac{F_{10}}{A_o} \quad (1)$$

where F_{10} is the force corresponding to a strain of 10 %, in newtons, and A_0 is the initial cross-sectional area of the specimen, in square millimeters.

For this test, the machine model TC050369, manufacturer LABOMAK, was used.

According to the standard BS EN 1604:2013 "Thermal insulating products for building applications - Determination of dimensional stability under specified temperature and humidity conditions" to calculate the dimensional changes, $\Delta\varepsilon_l$, $\Delta\varepsilon_b$, and $\Delta\varepsilon_d$, in percentage, from the individual measurements, using Eq. (2), Eq. (3) and Eq.(4):

$$\Delta\varepsilon_l = 100 \frac{l_t - l_0}{l_0} \quad (2)$$

$$\Delta\varepsilon_b = 100 \frac{b_t - b_0}{b_0} \quad (3)$$

$$\Delta\varepsilon_d = 100 \frac{d_t - d_0}{d_0} \quad (4)$$

where l_0, b_0, and d_0 are initial dimensions after conditioning, in mm, and l_t, b_t, and d_t are final dimensions, after exposure to temperature, in mm [12].

For the purpose of this test, the machine model BKHS120-2103004, manufacturer BLULAB, was used.

According to the standard BAS EN 12087:2014 "Thermal insulating products for building applications - Determination of long-term water absorption by immersion" test specimens need to be squares with squarely cut edges having sides of (200 ± 1) mm to calculate the water absorption after

the immersion time of 28 days, W28, in percent volume using formula (5):

$$W_{28} = 100\frac{m_{28}+V_1*\rho_w-m_0-m_1}{V_0*\rho_w} \quad (5)$$

where m_0 is the initial mass of the test specimen, in kilograms, m_1 is the mass of the empty cage immersed, in kilograms, m_{28} is the mass of the test specimen and the cage submerged after 28 days of immersion, in kilograms, $V_0 = l_0 \times b_0 \times d_0$ is the initial volume of the test specimen, in cubic meters, $V_1 = l_1 \times b_1 \times d_1$ is the volume of the test specimen after 28 days of immersion, in cubic meters, ρ_W is the density of water, assumed to be 1000 kg/m^3, W_{28} shall be rounded to the nearest 0.1 volume percent, [13]. All testing was carried out at (23 ± 5) °C (50 ± 5) % relative humidity.

3. RESULTS AND DISCUSSION

Three different types of sample testing were performed: compressive strength, dimensional stability under specified temperature and humidity conditions, and long-term water absorption by immersion. This study compared the results in relation to the following influences of process parameters: different MFI, different proportions of additives, and different surface finishes.

3.1. Different MFIs

From each XPS board, 5 samples of 100 x 100 mm dimensions were created. The samples are sampled in such a way that the entire board is tested across the width. The samples differ only in the type of granulate, while the other additives and parameter settings are the same or relatively the same. Granulate with an MFI of 3.5 g/10 min is in sample number 2, while granulate with an MFI range of 2.5 to 3 g/10 min is in sample number 1. Figures 1 and 2 show the force-displacement curves for samples 1 and 2. For Samples 1 and 2, five replicate tests were performed. Five specimens were cut from a single large board of the same composition and material properties, ensuring consistency among the tested specimens. Each specimen was tested separately, and the results shown in Figure 1 correspond to these five measurements as well as figure 2.

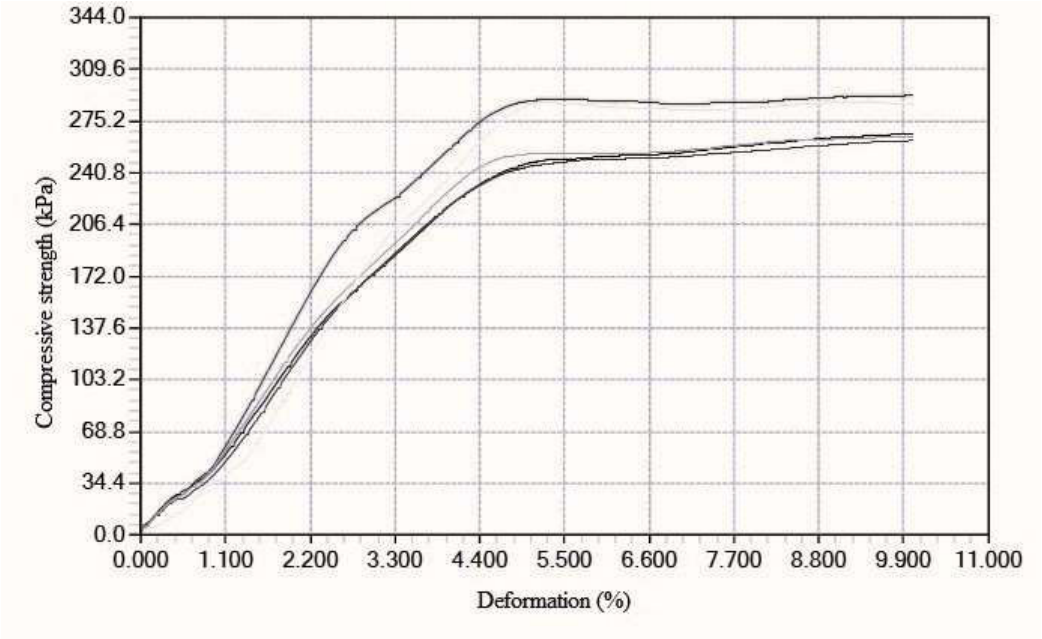

Figure 1. Compressive Strength–Defromation Diagram of sample 1.

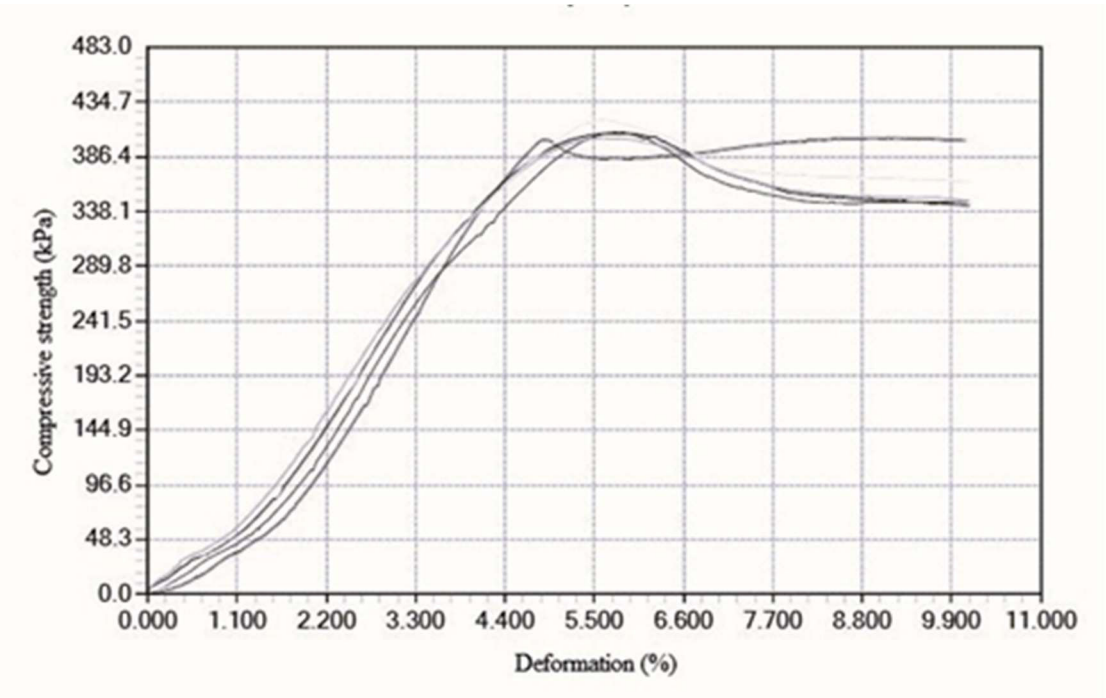

Figure 2. Compressive strength vs deformation of XPS sample of sample 2.

Table 1 shows the average values of mass, density, and compressive strength of the tested samples. All samples were tested on the day of their production.

Table 1. Average values of mass, density and compressive strength of samples 1 and 2

Sample	Mass (g)	Density (g/m^3)	Compressive strength (kPa)
1	14.98	30.32	274.8
2	16.19	32.87	407.9

By analyzing samples 1 and 2, we observe differences in all three parameters. The sample with a granulate whose MFI is 3.5 g/10 min shows higher compressive strength. Since a higher MFI means the material flows more easily when melted (lower viscosity) and a lower MFI means the material is more viscous and flows less easily, we can conclude that when the molten material flows more easily, better compressive strength results are obtained.

Also, better flow leads to a more homogeneous distribution of the polymer melt, resulting in a more uniform and dense cellular structure. This enhances compressive strength because the material is less prone to structural weaknesses. It should be noted that density itself is an indicator of compressive strength. Namely, the greater the mass of the sample and therefore the density, the compressive strength will always be higher than for samples with a lower mass. At the time of sampling, the difference in the material flow rate for samples 1 and 2 is insignificant and amounts to 6 kg/h or 1.3%. The observed differences in compressive strength confirm the critical role of MFI in the production of XPS insulation materials.

3.2. Different proportions of additives

The study further examined how varying the proportions of additives, particularly CO_2 and nucleating agent (H.N.), influences the physical properties of XPS panels. Table 2 shows the ratios of several raw materials, while Table 3 shows the average values of mass, density, and compressive strength of the tested samples.

All samples were tested on the day of their production. From each XPS board, 5 samples of 100 x 100 mm dimensions were created. The samples are sampled in such a way that the entire board is tested across the width.

Figures 3 and 4 show the force-displacement curves for samples 3 and 4.

For Samples 1 and 2, five replicate tests were performed. Five specimens were cut from a single large board of the same composition and material properties, ensuring consistency among the tested specimens. Each specimen was tested separately, and the results shown in Figures 1 and 2 correspond to these five measurements.

Table 2. Ratios of several raw materials

Sample	GPPS	H.N.	CO_2
3	91.04 %	0.16 %	1.36 %
4	90.98 %	0.12 %	1.12 %

Table 3. Average values of mass, density, and compressive strength of samples 3 and 4

Sample	Mass (g)	Density (g/m^3)	Compressive strength (kPa)
3	16.07	32.28	381.9
4	15.20	30.41	326.3

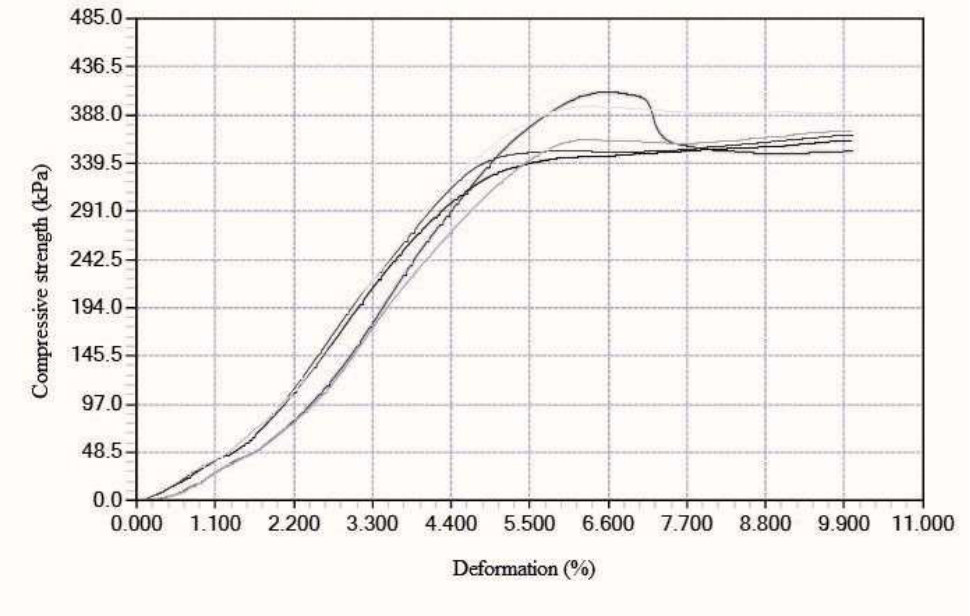

Figure 3. Compressive strength vs deformation of XPS sample 3

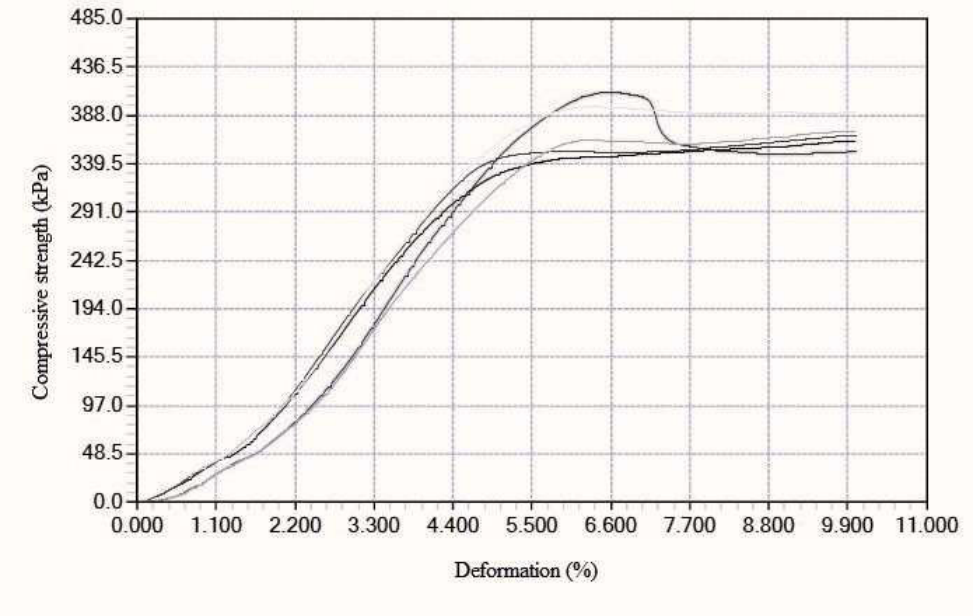

Figure 4. Compressive strength vs deformation of XPS sample 4

Analyzing the test results of samples 3 and 4, we see that by increasing the percentage of CO_2, as well as increasing H.N., the samples, and the extension XPS boards have better mechanical properties in the form of compressive strength.

These additives influence the cell structure of the foam, resulting in enhanced mechanical properties. However, careful optimization is required, as excessive additive concentrations may negatively impact other properties such as thermal insulation and long-term stability. The amount of CO_2 influences cell size and density. For example, too little CO_2 means fewer gas bubbles, denser foam, reduced insulation, but higher strength, and too much CO_2 means excessive expansion, larger cell size, and weaker structure.

The nucleating agent (H.N.) promotes smaller, more evenly distributed bubbles, leading to a denser foam with uniform cell structure, which improves compressive strength and a more stable material with lower risk of deformation over time.

The right balance of CO_2 and nucleating agents creates an optimal foam structure, increasing compressive strength without compromising insulation properties.

The proportion of GPPS in both samples is relatively the same as the specifications of the finished product and process parameters, except for the proportion of the additives already mentioned. Table 4 presents the relationship between additive proportions and compressive strength, demonstrating a direct correlation between increased CO_2 content and improved mechanical performance. From Table 4, we see that, in addition to the compressive strength, the mass and therefore the density of the sample with an increased proportion of the additives mentioned is greater. The total amount of input raw material for sample 4 is greater than sample 3 by 11.31 kg, which is approximately 1.18% of the total amount of input raw materials. Thus, sample 3 has a smaller amount of input raw materials at the time of sampling and a higher proportion of H.N. and CO_2.

3.3. Different surface finishes

After conditioning, three 200 x 200 mm samples are cut out from one XPS board. Table 4 shows the results of dimensional stability under specified temperature and humidity conditions, that is, the contraction

and expansion of samples. The results show the mean value of all three samples.
The samples were measured three times in length, three times in width, and five times in thickness. After that, the samples were placed in a drying oven at 60 °C for 48 hours. After conditioning, the samples were measured again at the same marked places. Using mathematical formulae (2), (3), and (4), the dimensional changes are calculated in percentage. Sample 5 has a surface with a waffle texture, while sample 6 has a surface with openings in channels. After conditioning, three 200 x 200 mm samples are cut out from one XPS board. Table 5 shows the results of long-term water absorption by immersion. The results show the mean value of all three samples. Sample 7 has a surface with a waffle texture, while sample 8 has a surface with openings in channels.

Table 4. Calculated dimensional changes of samples 5 and 6

Sample	$\Delta\varepsilon_l$	$\Delta\varepsilon_b$	$\Delta\varepsilon_d$
5	0.17 %	0.16 %	0.90 %
6	0.09 %	0.20 %	1.00 %

Table 5. Long-term water absorption by immersion of samples 7 and 8

Sample	W_{28}
7	1.37 %
8	1.09 %

4. CONCLUSION

The study confirms that process parameters play a crucial role in defining the physical and mechanical properties of XPS. The findings indicate that even minor variations in key parameters, such as the melt flow index (MFI), additive composition, and surface finish, can significantly affect the material's compressive strength, density, dimensional stability, and water absorption properties.
The key findings include:

1. MFI: Higher MFI results in improved compressive strength due to better material flow during processing;
2. Additive Proportions: Increased CO_2 and nucleating agent (H.N.) enhance the mechanical properties, including compressive strength and density;
3. Surface Finish: XPS panels with channel openings exhibit better dimensional stability and lower water absorption compared to waffle-textured surfaces.

To further refine the production and application of XPS, future studies should explore the long-term durability of different formulations under real-world conditions, including temperature fluctuations and prolonged exposure to moisture. Additionally, research into alternative foaming agents with lower environmental impact could help improve the sustainability of XPS production. Further investigations into the trade-offs between mechanical strength, thermal insulation, and process efficiency will be essential for optimizing the material for a broader range of applications in the construction and insulation industries.

Conflicts of Interest

The authors declare no conflict of interest.

REFERENCES

[1] S. Lee, R. Smith, S. Costeux, J. Alcott, M. Barger, D. Beaudoin, H. Clayton, S. Donati, J. Duffy, R. Fox, D. Frankowski, K. Giza, L. Hood, T. Hu, C. Kruse, T. Morgan, C. Shmidt, W. Stobby, C. Vo, Zero ozone- depleting foaming agent technology for extruded polystyrene

foam. FOAMS 2009 Conference – Iselin, NJ. Sept. 2009

[2] W. D. Callister, J. R, D. G. Rethwisch, *Materials Science and Engineering: An Introduction*, deseto izdanje 2018. United States of America 545 -563.

[3] S.-T. Lee, Chul B. Park. Foam Extrusion: Principles and Practice, 2nd ed., CRC Press, Boca Raton, Florida, USA, 2014.

[4] O. M.Yaghi, M. O'Keeffe, N. W. Ockwig, H. K. Chae, M. Eddaoudi, J. Kim, Reticular synthesis and the design of new materials. Nature, 2003, 423, 705-714. DOI: 10.1038/nature01650.

[5] Fang, J., Xuan, Y., & Li, Q. Preparation of polystyrene spheres in different particle sizes and assembly of the PS colloidal crystals. Science China Technological Sciences. 2010.

[6] Fashandi, H., & Karimi, M.. Characterization of porosity of polystyrene fibers electrospun at humid atmosphere. Thermochimica Acta. 2012.

[7] Cai, S.; Zhang, B.; Cremaschi, L. Review of moisture behavior and thermal performance of polystyrene insulation in building applications. Build. Environ. 2017

[8] Kilar, V., Koren, D., Bokan-Bosiljkov, V. Evaluation of the performance of extruded polystyrene boards—Implications for their application in earthquake engineering. Polym. Test. 2014.

[9] H Zhang. Scale-up of extrusion foaming process for manufacture of polystyrene foams using carbon dioxide. Graduate Department of Mechanical and Industrial Engineering University of Toronto. 2010.

[10] V.G. Krishnan, L. Fiorucci, A. Sarbu, W. Drenckhan-Andreatta. Characterizing the foaming process of polymers: review of experimental methods. Adv. Colloid Interface Sci., 344. 2025.

[11] Institute for Standardization of Bosnia and Herzegovina, BAS EN 826:2014, Thermal insulating products for building applications – Determination of compression behaviour, East Sarajevo, Bosnia and Herzegovina, 2014.

[12] Institute for Standardization of Bosnia and Herzegovina (ISBIH). (2014). BAS EN 1604:2014, Thermal insulating products for building applications – Determination of dimensional stability under specified temperature and humidity conditions. East Sarajevo, Bosnia and Herzegovina: ISBIH.

[13] Institute for Standardization of Bosnia and Herzegovina (ISBIH). (2014). BAS EN 12087:2014, Thermal insulating products for building applications – Determination of long-term water absorption by immersion. method 2C). East Sarajevo, Bosnia and Herzegovina: ISBIH.